STRUCTURAL CHEMISTRY
ISSN 2053-2296

Catalyst- and solvent-free synthesis of 2-fluoro-*N*-(3-methylsulfanyl-1*H*-1,2,4-triazol-5-yl)benzamide through a microwave-assisted Fries rearrangement: X-ray structural and theoretical studies

Rodolfo Moreno-Fuquen,[a]* Kevin Arango-Daraviña,[a] Diana Becerra,[b] Juan-Carlos Castillo,[b,c] Alan R. Kennedy[d] and Mario A. Macías[e]*

[a]Department of Chemistry, Universidad del Valle, AA 25360, Santiago de Cali, Colombia, [b]Grupo de Catálisis, Escuela de Ciencias Químicas, Universidad Pedagógica y Tecnológica de Colombia, UPTC, Avenida Central del Norte, Tunja, Colombia, [c]Bioorganic Compounds Research Group, Department of Chemistry, Universidad de los Andes, Carrera 1 No. 18A-10, Bogotá, Colombia, [d]WestCHEM, Department of Pure and Applied Chemistry, University of Strathclyde, 295 Cathedral Street, Glasgow G1 1XL, Scotland, and [e]Department of Chemistry, Universidad de los Andes, Carrera 1 No. 18A-12, 111711 Bogotá, Colombia. *Correspondence e-mail: rodolfo.moreno@correounivalle.edu.co, ma.maciasl@uniandes.edu.co

Received 18 December 2018
Accepted 20 February 2019

Edited by Y. Ohgo, Teikyo University, Japan

Keywords: Fries rearrangement; heterocyclic amides; crystal structure; amino-1,2,4-triazole; prototropy process; microwave-assisted reaction; DFT; computational chemistry; Hirshfeld surface maps.

CCDC references: 1898376; 1898375

Supporting information: this article has supporting information at journals.iucr.org/c

An efficient approach for the regioselective synthesis of (5-amino-3-methylsulfanyl-1*H*-1,2,4-triazol-1-yl)(2-fluorophenyl)methanone, $C_{10}H_9FN_4OS$, (3), from the *N*-acylation of 3-amino-5-methylsulfanyl-1*H*-1,2,4-triazole, (1), with 2-fluorobenzoyl chloride has been developed. Heterocyclic amide (3) was used successfully as a strategic intermediate for the preparation of 2-fluoro-*N*-(3-methylsulfanyl-1*H*-1,2,4-triazol-5-yl)benzamide, $C_{10}H_9FN_4OS$, (4), through a microwave-assisted Fries rearrangement under catalyst- and solvent-free conditions. Theoretical studies of the prototropy process of (1) and the Fries rearrangement of (3) to provide (4), involving the formation of an intimate ion pair as the key step, were carried out by density functional theory (DFT) calculations. The crystallographic analysis of the intermolecular interactions and the energy frameworks based on the effects of the different molecular conformations of (3) and (4) are described.

1. Introduction

Among the broad range of privileged structures, triazole represents one of the most prominent classes of N-heterocyclic scaffolds for novel synthetic drug discovery due to its broad range of pharmacological and biological activities (Jagdish *et al.*, 2013; Kantheti *et al.*, 2015; Nocentini *et al.*, 2016; Aneja *et al.*, 2018). Thought the triazole moiety has not been found in natural products, the development of efficient and straightforward methods for the preparation of triazole derivatives has greatly increased over the last two decades. This is one of the reasons why the five-membered triazole ring has been employed as a building block for the construction of more complex heterocyclic systems with innumerable applications in the pharmaceutical industry (Yu *et al.*, 2014; Häring *et al.*, 2018), medicinal chemistry (Trinh *et al.*, 2017; Giroud *et al.*, 2018) and agrochemicals (Singh & Dureja, 2000). In that sense, knowledge of the tautomeric preferences and the factors affecting its tautomeric equilibrium is important for understanding the reactivity of 1,2,4-triazole derivatives in chemical and enzymatic processes. In particular, the amino-1,2,4-triazole ring can exist in three tautomeric forms, namely, 3-amino-1*H*-1,2,4-triazole, (I), 3-amino-4*H*-1,2,4-triazole, (II), and 5-amino-1*H*-1,2,4-triazole, (III), as depicted in Scheme 1.

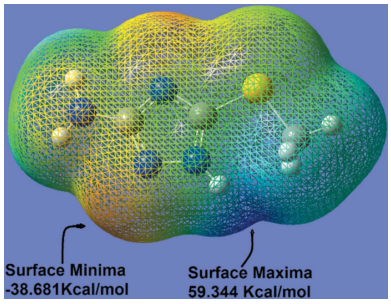

Theoretical and experimental studies of the tautomerism in amino-1,2,4-triazoles have demonstrated that only 1*H*-forms (I) and (III) exist rather than 4*H*-form (II) either in the solid state or in solution, as shown in Scheme 1 (Palmer & Christen, 2004; Ozimiński *et al.*, 2004; Karpińska & Dobrowolski, 2008; Dolzhenko *et al.*, 2009). In this context, Dolzhenko's group reported the catalyst-free synthesis and a tautomerism study of 3(5)-amino-5(3)-(het)aryl-1,2,4-triazoles in aqueous medium using NMR spectroscopy and X-ray crystallography (Dolzhenko *et al.*, 2009), showing that 5-amino-1*H*-1,2,4-triazoles, *i.e.* (III), were electronically preferred in the tautomeric equilibrium. However, theoretical studies on the tautomerism of amino-1,2,4-triazoles containing a methylsulfanyl group instead of the (het)aryl substituent has remained largely unexplored. On the other hand, 3-amino-5-methylsulfanyl-1*H*-1,2,4-triazole is also used for the synthesis of 1,2,4-triazole-fused heterocycles containing a methylsulfanyl group, including [1,2,4]triazolo[1,5-*a*]pyrimidines (Fischer, 2008), [1,2,4]triazolo-[1,5-*a*]pyrimidinones (Martins *et al.*, 2016), [1,2,4]triazolo[1,5-*a*]-[1,3,5]triazines (Dolzhenko *et al.*, 2006) and [1,2,4]triazolo[5,1-*c*]-[1,2,4]triazines (Hassan *et al.*, 2018). In addition, the synthesis of 1,2,4-triazole-fused heterocycles has received augmented interest in recent years due to their broad range of activities, including antimicrobial (Khalil, 2006; Aggarwal *et al.*, 2011), antitumour (El-Husseiny *et al.*, 2018), antifungal (Chohan & Hanif, 2013) and anticonvulsant (Almasirad *et al.*, 2004). Furthermore, it has been found that some *N*-benzoyl-1,2,4-triazoles possess a wide spectrum of activities, including as inhibitors of the receptor protein tyrosine kinase Axl (Singh *et al.*, 2007), as selective inhibitors of CDK1 and CDK2 (Connolly *et al.*, 2006), and anti-inflammatory activity (Abdel-Megeed *et al.*, 2009). Though a plethora of methods for the synthesis of this scaffold have been developed, there still remains a great need to find operationally simple, high-yielding and ecofriendly methodologies for the regioselective *N*-acylation of 3-amino-5-methylsulfanyl-1*H*-1,2,4-triazole, (1), which can be used as a building block for the preparation of biologically active [1,2,4]triazole-fused heterocycles. In this sense, *N*-benzoyl-1,2,4-triazoles are amenable to further derivatization *via* palladium-catalyzed substitutions of the methylsulfanyl moiety (Liebeskind–Srogl cross-coupling) (Liebeskind & Srogl, 2002). Continuing our ongoing research toward the synthesis of biologically active N-heterocycles using green-chemistry tools (Moreno-Fuquen *et al.*, 2014, 2015, 2017; Viana *et al.*, 2016; Castillo *et al.*, 2018*a*), we envisioned that the regioselective *N*-acylation of 3-amino-5-methylsulfanyl-1*H*-1,2,4-triazole, (1), with 2-fluorobenzoyl chloride, (2), might generate the amino-1,2,4-triazole (3) acylated on the triazolic ring, which upon microwave irradiation would provide the secondary amide (4) acylated on the exocyclic amine group *via* a Fries rearrangement under catalyst- and solvent-free conditions (Scheme 2). In the present work, the structures of the synthesized amides, the tautomerism and the mechanistic pathway were investigated using both theoretical studies and X-ray crystallography.

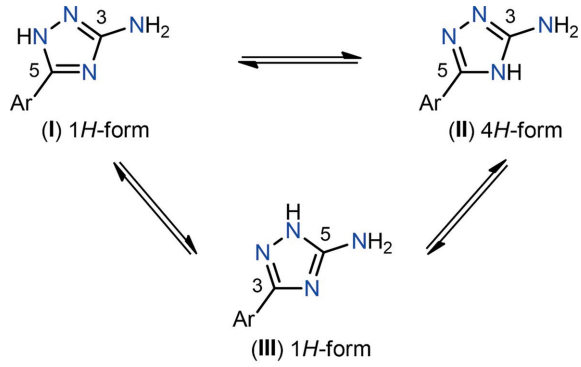

Scheme 1

2. Experimental

2.1. General information

All reagents were purchased from commercial sources and used without further purification unless otherwise noted. All starting materials were weighed and handled in air at room temperature. The reactions were monitored by thin-layer chromatography (TLC) visualized by UV lamp (254 nm or 365 nm). Flash chromatography was performed on silica gel (230–400 mesh). All reactions under microwave irradiation were performed in oven-dried 10.0 ml sealable Pyrex tubes equipped with a Teflon-coated stirring bar (obtained from CEM). Microwave-assisted reactions were performed in a CEM Discover SP focused microwave (ν = 2.45 GHz) reactor

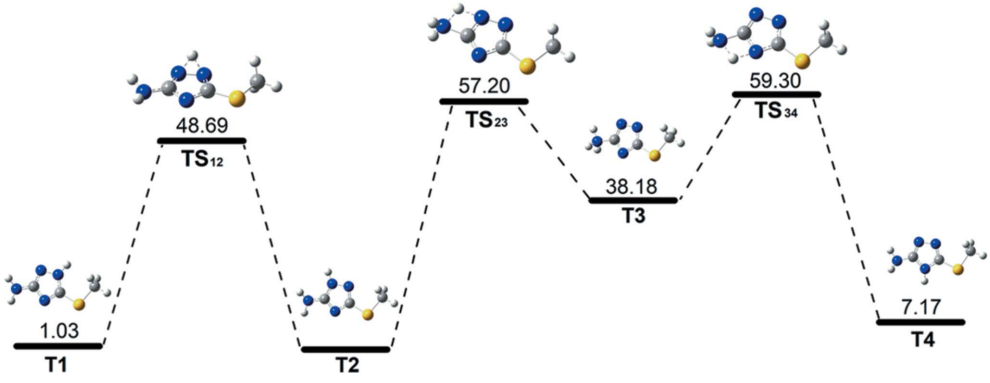

Figure 1
Theoretical study of the prototropy process in amino-1,2,4-triazole (1). The energy profile was computed at the B3LYP/6-311++G(d,p) level. Energy values are in kcal mol^{-1}.

Table 1
Experimental details.

	(3)	(4)
Crystal data		
Chemical formula	$C_{10}H_9FN_4OS$	$C_{10}H_9FN_4OS$
M_r	252.27	252.27
Crystal system, space group	Triclinic, $P\overline{1}$	Monoclinic, $P2_1/n$
Temperature (K)	298	298
a, b, c (Å)	7.6599 (9), 7.8079 (8), 10.0140 (12)	5.0509 (11), 26.640 (5), 8.0251 (16)
α, β, γ (°)	94.487 (9), 108.668 (11), 97.565 (9)	90, 94.12 (2), 90
V (Å^3)	557.83 (12)	1077.0 (4)
Z	2	4
Radiation type	Mo $K\alpha$	Mo $K\alpha$
μ (mm^{-1})	0.29	0.30
Crystal size (mm)	0.38 × 0.34 × 0.22	0.23 × 0.08 × 0.05
Data collection		
Diffractometer	Agilent SuperNova Dual Source diffractometer with an Atlas detector'	Agilent SuperNova Dual Source diffractometer with an Atlas detector
Absorption correction	Multi-scan (*CrysAlis PRO*; Agilent, 2014)	Multi-scan (*CrysAlis PRO*; Agilent, 2014)
T_{min}, T_{max}	0.856, 1.000	0.734, 1.000
No. of measured, independent and observed $[I > 2\sigma(I)]$ reflections	12256, 2450, 2107	5060, 5060, 3267
R_{int}	0.044	0.080
$(\sin\theta/\lambda)_{max}$ (Å^{-1})	0.641	0.634
Refinement		
$R[F^2 > 2\sigma(F^2)]$, $wR(F^2)$, S	0.042, 0.116, 0.89	0.071, 0.237, 1.10
No. of reflections	2450	5060
No. of parameters	225	165
No. of restraints	159	0
H-atom treatment	H atoms treated by a mixture of independent and constrained refinement	H atoms treated by a mixture of independent and constrained refinement
$\Delta\rho_{max}$, $\Delta\rho_{min}$ (e Å^{-3})	0.27, −0.22	0.29, −0.38

Computer programs: *CrysAlis PRO* (Agilent, 2014), *SUPERFLIP* (Palatinus & Chapuis, 2007), *SHELXL2014* (Sheldrick, 2015) and *Mercury* (Macrae *et al.*, 2008).

equipped with a built-in pressure measurement sensor and a vertically focused IR temperature sensor. Controlled temperature, power and time settings were used for all reactions. NMR spectra were recorded at 400 (^{1}H), 376 (^{19}F) and

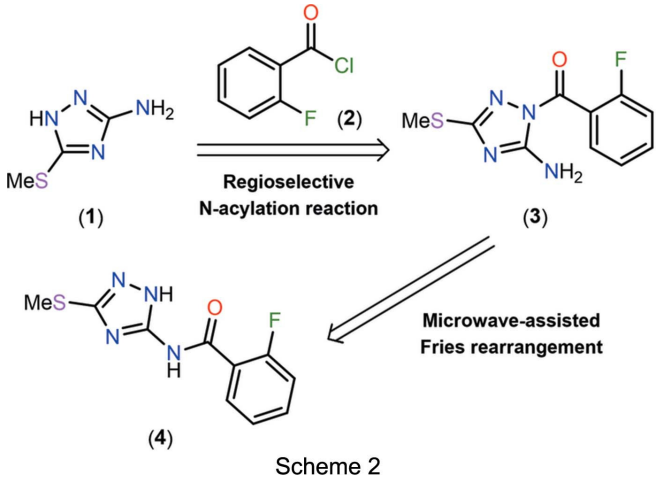

Scheme 2

101 MHz (^{13}C) at 298 K using tetramethylsilane (0 ppm) as the internal reference. NMR spectroscopic data were recorded in $CDCl_3$ or DMSO-d_6 using as internal standards the residual nondeuterated signal for ^{1}H NMR and the deuterated solvent signal for ^{13}C NMR spectroscopy. DEPT spectra were used for the assignment of carbon signals. Chemical shifts (δ) are given in ppm and coupling constants (J) are given in Hz. The following abbreviations are used for multiplicities: s = singlet, d = doublet, t = triplet, q = quartet, dd = doublet of doublets and m = multiplet. Melting points were determined using a capillary melting-point apparatus and are uncorrected. IR spectra were recorded on an FT–IR spectrophotometer using KBr disks. Spectra are reported in wavenumbers (cm^{-1}) and only selected resonances are reported. High-resolution mass spectra (HRMS) were recorded using a Q-TOF spectrometer *via* electrospray ionization (ESI). UV–Vis measurements were performed in acetonitrile as solvent at room temperature (293 K).

2.2. Synthesis and crystallization

2.2.1. Synthesis of (5-amino-3-methylsulfanyl-1*H*-1,2,4-triazol-1-yl)(2-fluorophenyl)methanone, (3) (Scheme 2). 2-Fluorobenzoyl chloride, (2) (478 µl, 4.0 mmol), was added dropwise to a solution of 3-amino-5-methylsulfanyl-1*H*-1,2,4-triazole, (1) (521 mg, 4.0 mmol), and triethylamine (668 µl, 4.8 mmol) in dichloromethane (5.0 ml). The mixture was stirred at room temperature for 1 h until the starting materials were no longer detected by TLC. After the solvent was removed under reduced pressure, water (5.0 ml) was added and the aqueous solution was extracted with ethyl acetate (2 × 5.0 ml). The combined organic layers were dried with anhydrous magnesium sulfate and the solvent was removed under reduced pressure to afford compound (3) as a white solid

[yield 948 mg, 94%; m.p. 428–429 K (amorphous), literature 430–432 K (Somorai *et al.*, 1986)]. Recrystallization of (3) from methanol afforded white crystalline prisms suitable for single-crystal X-ray diffraction analysis. FT–IR (KBr): ν = 3429 (NH_2), 3282 (NH_2), 3101, 3070, 2927, 1689 (C═O), 1643 (C═N), 1612 (C═C), 1489, 1342, 1257, 1230, 933, 748, 659 cm^{-1}. ^1H NMR (400 MHz, $CDCl_3$): δ 2.43 (*s*, 3H, SCH_3), 6.99 (*br s*, 2H, NH_2), 7.17 (*t*, J = 9.2 Hz, 1H), 7.24 (*t*, J = 7.4 Hz, 1H), 7.51–7.57 (*m*, 1H), 7.69 (*td*, J = 2.0, 7.7 Hz, 1H). ^{19}F NMR (376 MHz, $CDCl_3$): δ −109.9. $^{13}C\{^1H\}$ NMR (101 MHz, $CDCl_3$): δ 13.6 (SCH_3), 116.3 (CH, *d*, J_{C-F} = 21.3 Hz), 121.5 (C, *d*, J_{C-F} = 13.5 Hz), 123.8 (CH, *d*, J_{C-F} = 3.6 Hz), 130.8 (CH, *d*, J_{C-F} = 0.7 Hz), 133.9 (CH, *d*, J_{C-F} = 8.7 Hz), 158.1 (C), 160.2 (C, *d*, J_{C-F} = 256.9 Hz), 163.1 (C), 165.2 (C). The UV–Vis spectrum of (3) (10 µ*M*) was obtained in acetonitrile with λ_{max} of 240 (0.56 of absorption) and 283 nm (0.27 of absorption). HRMS (ESI+) calculated for $C_{10}H_{10}FN_4OS^+$: 253.0559 [M + H]$^+$; found: 253.0577 (see supporting information).

2.2.2. Synthesis of 2-fluoro-*N*-(3-methylsulfanyl-1*H*-1,2,4-triazol-5-yl)benzamide, (4) (Scheme 2). A 10 ml sealable oven-dried tubular reaction vessel was charged with compound (3) (63 mg, 0.25 mmol) and subjected to microwave irradiation at 453 K for 20 min, after which the reaction mixture was cooled to 328 K by air flow. The resulting crude product was purified by flash chromatography on silica gel using a mixture of CH_2Cl_2 and MeOH (30:1 *v*/*v*) as eluent to give (4) as a white solid [yield 53 mg, 84%; m.p. 472–473 K (amorphous), literature 480–482 K (Somorai *et al.*, 1986)]. Recrystallization of (4) from methanol afforded white prisms suitable for single-crystal X-ray diffraction analysis. FT–IR (KBr): ν = 3321, 3109, 2920, 1658 (C═O), 1581, 1546, 1462, 1369, 1284, 1234, 756, 624 cm^{-1}. ^1H NMR (400 MHz, DMSO-d_6): δ 2.49 (*s*, 3H, SCH_3), 7.30–7.36 (*m*, 2H), 7.58–7.62 (*m*, 1H), 7.69 (*t*, J = 7.6 Hz, 1H), 12.03 (*br s*, 1H, NH), 13.61 (*br s*, 1H, NH). ^{19}F NMR (376 MHz, DMSO-d_6): δ −113.6. $^{13}C\{^1H\}$ NMR (101 MHz, DMSO-d_6): δ 13.7 (SCH_3), 116.4 (CH, *d*, J_{C-F} = 21.7 Hz), 122.4 (C, *d*, J_{C-F} = 13.8 Hz), 124.6 (CH, *d*, J_{C-F} = 3.6 Hz), 130.2 (CH), 133.8 (CH, *d*, J_{C-F} = 8.6 Hz), 149.0 (C), 157.5 (C), 159.3 (C, *d*, J_{C-F} = 256.9 Hz), 163.0 (C). The UV–Vis spectrum of (4) (10 µ*M*) was obtained in acetonitrile with λ_{max} of 224 (0.61 of absorption) and 269 nm (0.30 of absorption). HRMS (ESI+) calculated for $C_{10}H_{10}FN_4OS^+$: 253.0559 [M + H]$^+$; found: 253.0577 (see supporting information). It is important to mention that the synthesis of secondary amide (4) from starting materials (1) and (2) was not possible with either conventional or dielectric heating. Though (3) was found to be unreactive at room temperature, the microwave-assisted reaction performed at 453 K for 20 min allowed the synthesis of secondary amide (4) in 84% isolated yield. Notably, by-products were not detected from the ^1H NMR spectrum of the crude reaction mixture.

2.3. Computational details

The geometry optimization of the tautomeric structures T1, T2, T3 and T4 were performed using a density functional theory (DFT) Becke three-parameter hybrid function with the nonlocal correlation of the Lee–Yang–Parr (B3LYP) method in the gas phase (Hohenberg & Kohn, 1964; Becke, 1993; Lee *et al.*, 1988). The corresponding harmonic vibrational frequencies were computed at the same level of theory to characterize them as minima (no imaginary frequencies) using the *GAUSSIAN09* program package (Frisch *et al.*, 2009). All the above calculations, including zero-point energy (ZPE) corrections, were performed at the 6-311++G(d,p) level of theory. Theoretical calculations to study the mechanistic pathway for the formation of (4) from (3) were performed in the gas phase at the B3LYP/6-31G level of theory.

2.4. Refinement

Crystal data, data collection and structure refinement details are summarized in Table 1. H atoms were placed in calculated positions for both compounds (C—H = 0.93–0.96 Å) and included as riding contributions, with isotropic displacement parameters set at 1.2–1.5 times the U_{eq} value of the parent atom. H atoms belonging to N—H groups were located in difference density maps and were refined freely. Single crystals of both compounds suitable for diffraction analysis were grown *via* slow evaporation from methanol at room temperature. The crystal structures were solved using an iterative algorithm (Palatinus & Chapuis, 2007) and subsequently completed by a difference Fourier map and refined using the program *SHELXL2014* (Sheldrick, 2015).

3. Results and discussion

3.1. Synthesis of (5-amino-3-methylsulfanyl-1*H*-1,2,4-triazol-1-yl)(2-fluorophenyl)methanone, (3)

At the origin of this work, it was hypothesized that 3-amino-5-methylsulfanyl-1*H*-1,2,4-triazole, (1), would be a suitable candidate for the regioselective *N*-acylation reaction with 2-fluorobenzoyl chloride, (2), to furnish amino-1,2,4-triazole (3) acylated on the triazolic ring (Scheme 2). In order to test that idea, a mixture of compounds (1) and (2) was completely dissolved in dichloromethane at ambient temperature, triethylamine (1.2 equivalents) was added and the solution was stirred for 1 h until completion (TLC control). Gratifyingly, tertiary amide (3) was obtained in 94% isolated yield as a single regioisomer. After analysis by X-ray diffraction and spectroscopic techniques (*i.e.* FT–IR, 1D NMR and HRMS spectroscopy), the formation of tertiary amide (3) was confirmed. Although compound (3) is a known molecule (Somorai *et al.*, 1986), no details about its spectroscopic and crystallographic analysis could be found. For that reason, a complete analytical and spectroscopic characterization was performed in this work (see *Experimental*). The main spectroscopic features of the structure of tertiary amide (3) corresponded to the presence of NH_2 and C═O absorption bands at 3429/3282 and 1689 cm^{-1}, respectively, in the IR spectrum. The most relevant features of the ^1H NMR spectrum of (3) corresponded to four different aromatic protons in the range of 7.17–7.69 ppm, as well as a broad singlet at 6.99 ppm associated with the NH_2 protons and the absence of

Table 2
Calculated energy (Hartrees), energy difference (ΔE) relative to T2, zero-point energy (ZPE) and total dipole moment (D) for tautomers T1, T2, T3 and T4, and transition states TS_{12}, TS_{23} and TS_{34} in the gas phase.

$E = E_{electr} + ZPE + E_{vib} + E_{rot} + E_{trans}$

Tautomer/ transition state	Calculated energy	ΔE (kcal mol^{-1})	ZPE	Dipole moment (D)
T1	−735.2403243	1.03	0.104679	3.22
T2	−735.2419592	0.00	0.104671	3.94
T3	−735.1820171	38.18	0.105567	8.39
T4	−735.2301485	7.17	0.104283	3.72
TS_{12}	−735.1592070	48.69	0.099515	1.19
TS_{23}	−735.1461367	57.20	0.100009	5.38
TS_{34}	−735.1424800	59.30	0.099699	5.20

the triazolic proton signal, confirming that the *N*-acylation reaction occurred on the triazolic ring instead of the exocyclic amino group. The presence of the SCH_3 signal at 13.6 ppm, four aromatic C atoms (═CH), four quaternary C atoms and the carbonyl group (C═O) at 165.2 ppm in the ^{13}C NMR spectrum agrees with the proposed structure for tertiary amide (3).

In order to rationalize the regioselectivity of the *N*-acylation reaction between 3-amino-5-methylsulfanyl-1*H*-1,2,4-triazole, (1), and 2-fluorobenzoyl chloride, (2), theoretical studies of the tautomeric equilibrium of (1) were carried out by DFT calculations. Particularly, the 1,2,4-triazole is a five-membered azole nucleus composed of three N atoms, which are involved in a prototropy process throughout the ring, allowing the possibility of acylation in these N atoms. For this reason, it is important to study the tautomeric equilibrium of (1) by DFT calculation in order to determine the relative stability of these tautomeric forms. Initially, we proposed that amino-1,2,4-triazole (1) can exist in four tautomeric forms, denoted T1, T2, T3 and T4 (Fig. 1). The prototropy process of amino-1,2,4-triazole (1) was then examined by DFT theoretical calculations of these tautomeric forms in the gas phase using the B3LYP functional with the extended base set 6-311++G(d,p) (Fig. 1). From this study, it was proposed that tautomer T1 suffered a proton shift from N1—H to N2 to form tautomer T2 *via* the transition state TS_{12} (activation barrier of 47.66 kcal mol^{-1}; 1 kcal mol^{-1} = 4.184 kJ mol^{-1}). The proton shift from N2—H to $-NH_2$ then afforded tautomer T3 *via* the transition state TS_{23} (activation barrier of 57.20 kcal mol^{-1}). Finally, a third proton shift from $-NH_3^+$ to N3 generated tautomer T4 *via* the transition state TS_{34} (activation barrier of 21.12 kcal mol^{-1}) (Fig. 1). Furthermore, the order of stability of the tautomers from most to least stable in terms of relative energy (given in kcal mol^{-1}) is T2 (0.00) > T1 (1.03) > T4 (7.17) > T3 (38.18), as depicted in Fig. 1. In conclusion, the prototropy process of (1) involved only tautomeric forms T1 and T2 with a high transition state energy TS_{12}, which are in agreement with previous experimental and theoretical studies (Sorescu *et al.*, 1998; Dolzhenko *et al.*, 2009; Shibl *et al.*, 2011).

On the basis of the aforementioned results and literature precedents (Fidler *et al.*, 1980; Reiter *et al.*, 1987; Dżygiel *et al.*, 2002), a plausible mechanism was proposed for the efficient and regioselective synthesis of tertiary amide (3) at ambient temperature using dichloromethane as a relatively nonpolar solvent and triethylamine as base (Scheme 3). Previously, we found by DFT calculations in the gas phase that tautomers T1 and T2 were the most stable in terms of relative energy and the tautomeric equilibrium involved a high transition state energy TS_{12}, as detailed in Table 2. It is important to mention that the high activation barrier from T1 to T2, and the regioselective formation of tertiary amide (3) in high yield would demonstrate that precursor (1) only exists in tautomeric form T1 at low temperature.

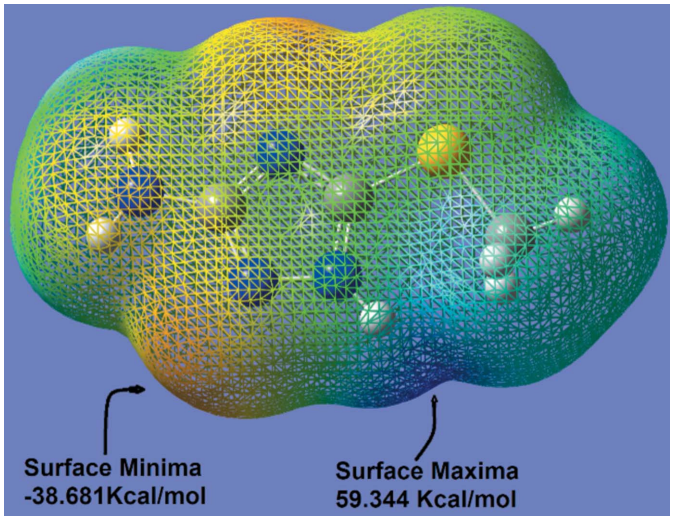

Figure 2
The molecular electrostatic potential (MEP) surface of tautomer T1.

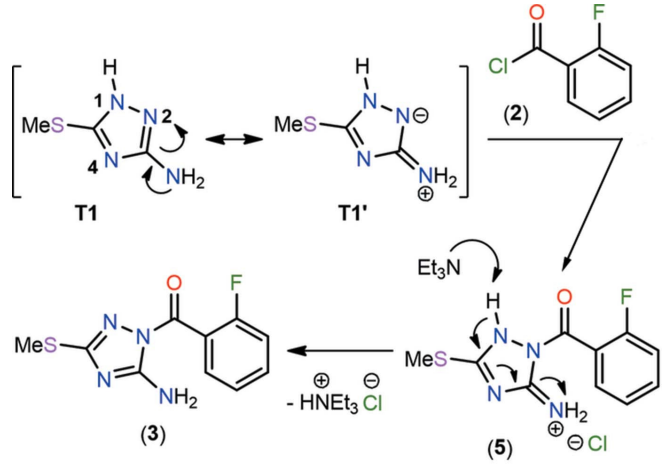

Scheme 3

In order to rationalize the reactivity of tautomer T1 in nucleophilic acyl substitution reactions, we decided to obtain the molecular electrostatic potential (MEP) surface of tautomer T1, as shown in Fig. 2. Thus, the N2 atom showed a negative potential (red) placed at the triazole moiety, with the positive potential (blue) located at the H atom attached to the N1 atom. This fact highlights the N2 atom as being responsible for the regioselective nucleophilic process instead of the exocyclic amine group.

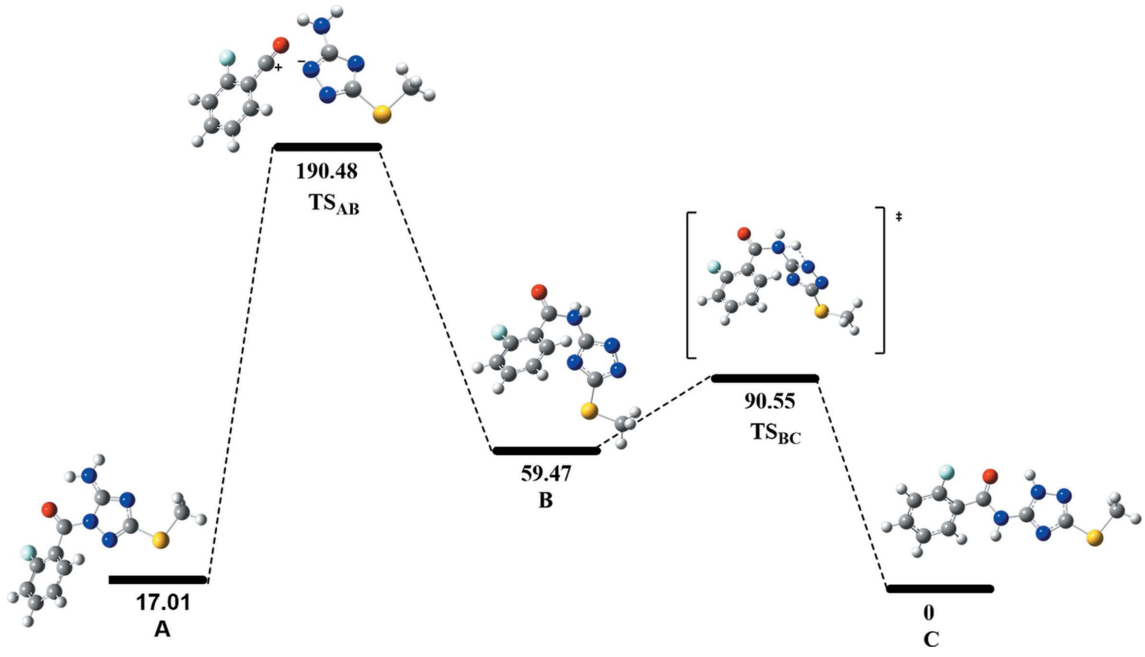

Figure 3
Theoretical study of the Fries rearrangement of (3) by the formation of an ion pair as the key step. The energy profile was computed at the B3LYP/6-31G level in the gas phase. Energy values are in kcal mol^{-1}.

A plausible mechanism for the regioselective synthesis of (3) is shown in Scheme 3. Initially, we proposed that tautomer T1 can be drawn in zwitterionic form T1″ containing a negative charge located on the N2 atom, which is in agreement with our theoretical studies of the molecular electrostatic potential (MEP) surface for tautomer T1 (Fig. 2). Consequently, zwitterionic form T1″ could explain the high nucleophilicity of the N2 atom, allowing the nucleophilic acyl substitution reaction with 2-fluorobenzoyl chloride, (2), to generate iminium salt (5) *via* a transient tetrahedral intermediate. Deprotonation of intermediate (5) by triethylamine then restores the aromaticity of the ring to give amide (3) in a regioselective manner.

3.2. Synthesis of 2-fluoro-*N*-(3-methylsulfanyl-1*H*-1,2,4-triazol-5-yl)benzamide, (4)

The synthesis of heterocyclic amides have received augmented interest in recent years due to their broad range of applications in drug design and medicinal chemistry. Traditional methods for the synthesis of heterocyclic amides include the use of activated carboxylic acids, such as anhydrides or acyl chlorides, as well as the use of stoichiometric amounts of coupling agents (Ojeda-Porras & Gamba-Sánchez, 2016). Although such methodologies are generally reliable, many of them involved harsh reaction conditions, prolonged reaction times and tedious work-up, and often proceed with low to moderate yields (Krause *et al.*, 2016). Although some reports are devoted to the synthesis of amides (3) through the regioselective *N*-acylation on the 1,2,4-triazole ring, the microwave-assisted chemical transformation of (3) to (4) *via* a Fries rearrangement has been poorly explored (Table 3 and Scheme 4). Despite the success of the Fries rearrangement of esters to obtain *o*-hydroxyphenones, we are surprised that few examples of the Fries rearrangement starting from simple amides have been described. The majority of these methods involve a photochemical excitation using a low-pressure Hg lamp (Ferrini *et al.*, 2007) and require the use of stoichiometric amounts of Brønsted or Lewis acids (Balkus *et al.*, 1998), prolonged reaction times, and tedious work-up. Nowadays, microwave-assisted synthesis has proved to be an extremely powerful tool because innumerable synthetic transformations and bond-forming steps can be carried out in a single-step (Kappe, 2008). Following our interest in this field (Castillo *et al.*, 2018*b*; Insuasty *et al.*, 2013; Acosta *et al.*, 2015; Macías *et al.*, 2018*a*), we envisioned that the microwave-assisted Fries rearrangement of tertiary amide (3) might generate secondary amide (4) through a catalyst- and solvent-free approach. Initially, the optimization was performed by varying the temperature and the solvent, and testing the effect of conventional heating *versus* microwave irradiation. Heating to reflux of (3) in tetrahydrofuran or toluene for 6 h provided secondary amide (4) in 15 and 31% yield, respectively (Table 3, entries 1 and 2). These preliminary results, showed that higher

Table 3
Optimization of the reaction conditions for the synthesis of secondary amide (4)[a].

Entry	Solvent	*T* (K)	Time *t*	Yield[b] (%)
1	THF	Reflux[c]	6 h	15
2	PhMe	Reflux[c]	6 h	31
3[d]	–	413	10 min	19
4[d]	–	433	10 min	42
5[d]	–	453	10 min	69
6[d]	–	453	20 min	84

Notes: (*a*) reaction conditions: tertiary amide (3) (0.25 mmol); (*b*) isolated yield; (*c*) conventional heating; (*d*) run in 10.0 ml sealed tubes at a power of 300 W in the absence of solvent.

temperatures favour the Fries rearrangement of the precursor (3). In a modified protocol, we performed the microwave-assisted reaction of (3) under catalyst- and solvent-free conditions at temperatures between 413 and 453 K for 10 min (Table 3, entries 3–5). To our delight, the highest yield (69%) was achieved at 453 K for 10 min. It should be noted that increasing the reaction time to 20 min led to desired product (4) in 84% yield (Table 3, entry 6). This microwave-assisted methodology for obtaining secondary amide (4) *via* a Fries rearrangement offers marked improvements in terms of efficacy, simplicity and eco-compatibility.

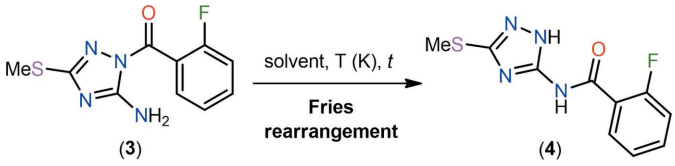

Scheme 4

The structure of (4) was confirmed by single-crystal X-ray diffraction analysis. Although compound (4) was reported three decades ago (Somorai *et al.*, 1986), no spectroscopic or crystallographic analysis details could be found. For that reason, a complete analytical and spectroscopic characterization (*i.e.* FT–IR, 1D NMR and HRMS spectroscopy) was performed in this work (see *Experimental*). The presence of broad absorption bands at 3321 and 1658 cm^{-1} assigned to the N—H and C═O groups, respectively, are the most relevant features of the IR spectrum. The presence of a low-field NH signal at 13.61 ppm and a broad singlet at 12.03 ppm associated with the NH proton of the new peptide bond formed are the most relevant features of the ^{1}H NMR spectrum. The presence of the SCH_3 signal at 13.7 ppm, four aromatic C atoms (═CH), four quaternary C atoms and the carbonyl (C═O) group at 163.0 ppm are the most relevant features of the ^{13}C NMR spectrum. A plausible mechanism for the catalyst- and solvent-free microwave-assisted synthesis of secondary amide (4) through a Fries rearrangement is shown in Scheme 5. The irradiation of microwave energy to (3) under optimized conditions can be efficiently absorbed due to its high dipolar momentum (8.82 D). This energy stimulates molecular rotational motions in the order of 1×10^{10} rotations per sec. Extra rotational energies result in strong friction between molecules (intermolecular collisions), raising the kinetic energy of the system (thermal energy) beyond the

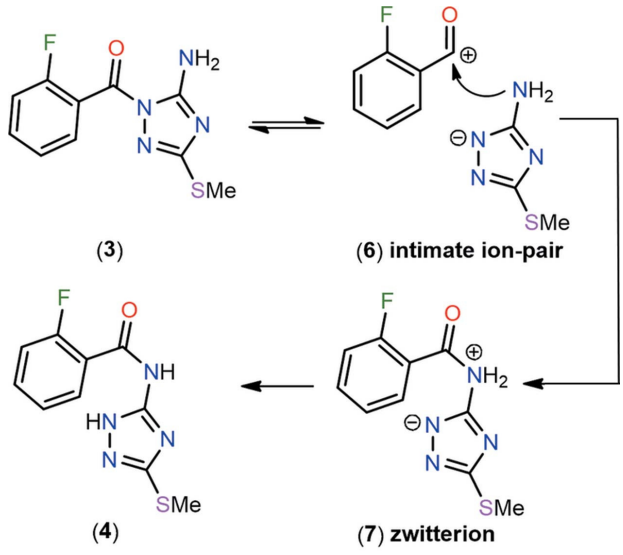

Scheme 5

melting temperature of the solid. The bonds of the molecule affected by rotations augment their vibrational displacements, and these bonds end up collapsing as a result of the thermal energy developed in the process. The MEP analysis of (3) and its high dipolar momentum indicate that the most affected bond in the molecule could be C7—N2, whose rupture would lead to the formation of an intimate ion pair, *i.e.* (6), under catalyst- and solvent-free conditions (Scheme 5). Then, nucleophilic addition of the NH_2 group of the 1,2,4-triazole anion on the acylium carbocation would generate zwitterionic intermediate (7), followed by a proton-transfer process to give secondary amide (4). The high temperature (453 K) and the absence of solvent could support our mechanistic proposal involving the formation of intimate ion pair (6) as the key step. For that reason, the postulated mechanism was examined by DFT theoretical calculations using the B3LYP functional with the extended basis set 6-31G in the gas phase, as depicted in Fig. 3.

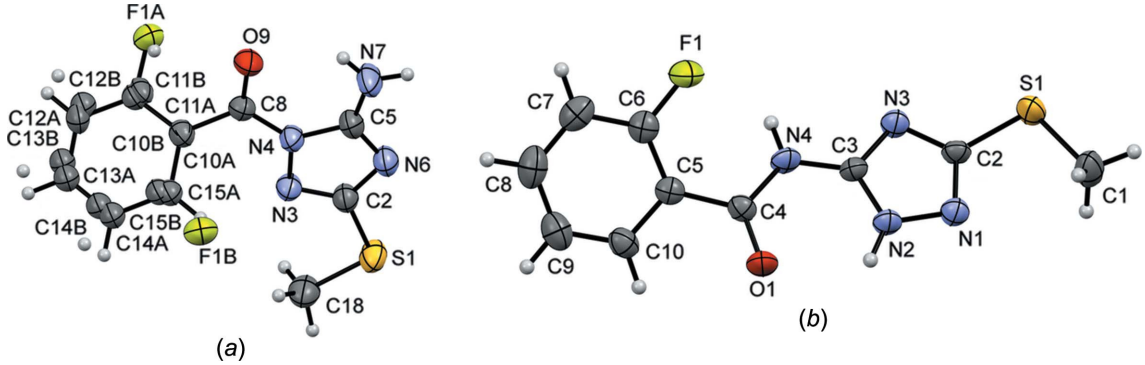

Figure 4
The molecular structures of (*a*) compound (3) and (*b*) compound (4), showing anisotropic displacement ellipsoids at the 50% probability level. The fluorophenyl ring in compound (3) shows positional disorder with refined values of 0.633 (3) and 0.367 (3) for fragments *A* (atoms connected by solid lines) and *B*, respectively.

The calculated mechanistic pathway shows that irradiation of sufficient microwave energy to compound (3) can achieve the fusion of the solid (428 K) and reach its dissociation in charged particles. The excitation of different rotational modes in (3) can increase the kinetic energy, achieving the formation of an intimate ion pair TS_{AB}, as depicted in Fig. 3. This ionic interaction can be seen as a dynamic process in equilibrium, where their reactivity can recover previously broken bonds or form a new bond between the NH_2 group of the 1,2,4-triazole anion and the acylium carbocation to give zwitterion *B via* the transition state TS_{AB} (activation barrier of 173.47 kcal mol^{-1}). Finally, intermediate *B* can participate in a prototropic process by transferring a proton from the exocyclic amine group to the N2 atom to afford the desired product *C via* the transition state TS_{BC} (activation barrier of 31.08 kcal mol^{-1}). The outcome of this reaction can be compared with a microwave-assisted Fries rearrangement under catalyst- and solvent-free conditions (Moghaddam *et al.*, 1999; Chouke & Ingle, 2012), where a free and stable acylium carbocation generated *in situ* can suffer a transposition from the triazolic C—N to the exocyclic C—N bond. This transposition generated by rotational motion promotes the reaction towards the formation of the desired product (4). The thermodynamic results derived from computational calculations showed a better stability of secondary amide (4) with respect to (3), as well as an irreversible tendency of the process, observing that the maximum temperature of the process did not exceed the fusion temperature of secondary amide (4). Though intramolecular N-to-N acyl transfer and intermolecular mechanisms were analyzed as possible reaction pathways, they were discarded considering that the optimized conditions needed to obtain (4) included high temperature (453 K) and the absence of solvent and catalyst.

3.3. Crystal structure analysis and energy frameworks

The crystal structures of the two prepared *N*-benzoyl-1,2,4-triazoles were analyzed. The molecules are characterized by

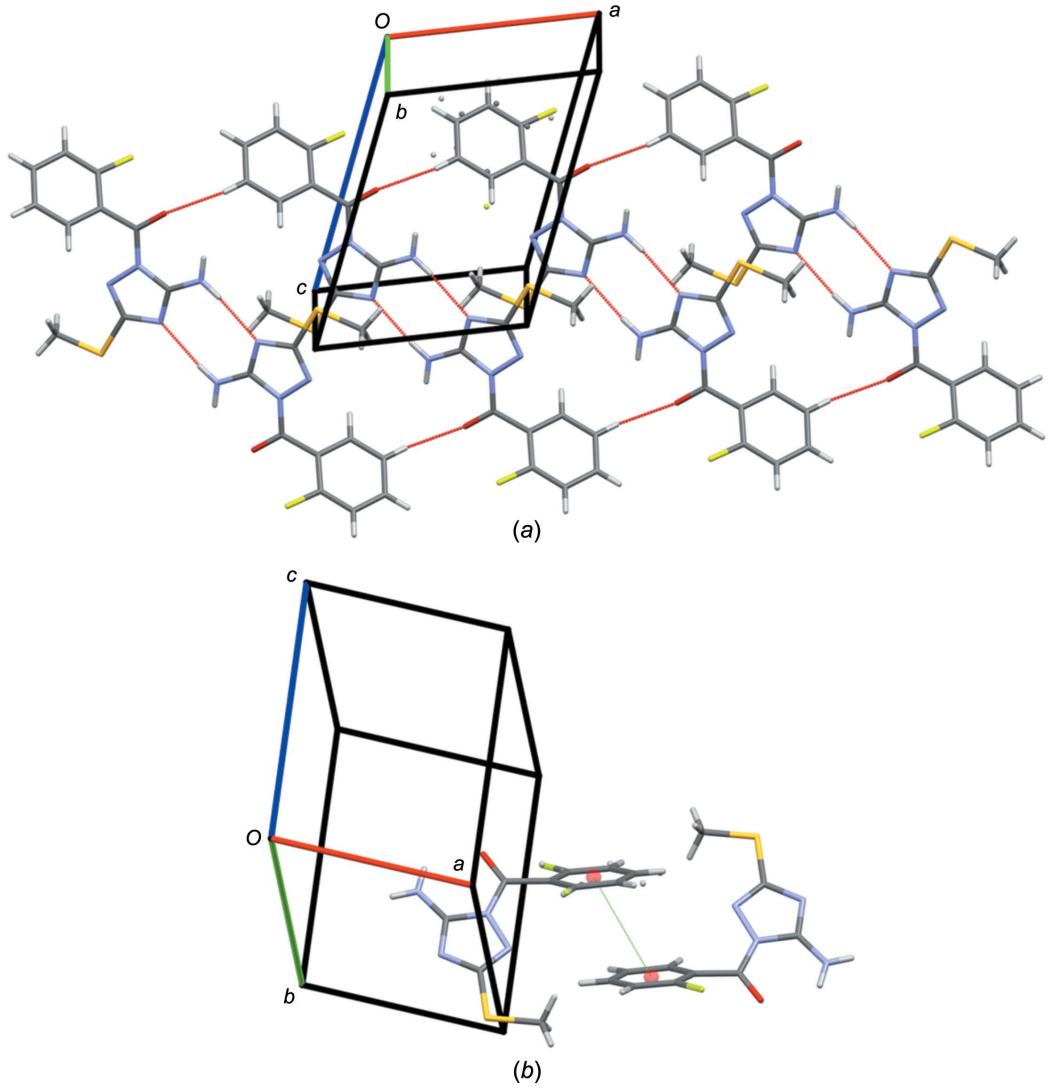

Figure 5
The crystal structure of (3), showing (*a*) the (N,C)—H···(N,O) hydrogen-bond interactions forming molecular chains along the [100] direction and (*b*) π–π interactions along the [010] direction.

Table 4
Hydrogen-bond geometry (Å, °) for (3).

D—H···A	D—H	H···A	D···A	D—H···A
N7—H1···O9	0.86 (1)	2.14 (2)	2.738 (2)	126 (2)
N7—H2···N6^{i}	0.86 (2)	2.13 (2)	2.987 (3)	174 (2)
C14A—H14A···O9^{ii}	0.93	2.36	3.275 (4)	167

Symmetry codes: (i) $-x+3, -y+1, -z+2$; (ii) $x-1, y, z$.

Table 5
Hydrogen-bond geometry (Å, °) for (4).

D—H···A	D—H	H···A	D···A	D—H···A
N4—H1···F1	0.92 (7)	2.25 (6)	2.710 (5)	111 (5)
N2—H4···O1	0.92 (10)	2.16 (8)	2.664 (5)	114 (7)
N4—H1···O1^{i}	0.92 (7)	2.13 (8)	3.013 (6)	159 (5)
N2—H4···N3^{ii}	0.92 (10)	2.17 (10)	2.926 (7)	140 (8)
C10—H10···O1^{iii}	0.93	2.58	3.367 (7)	143
C1—H1A···N1^{iv}	0.96	2.78	3.566 (8)	140

Symmetry codes: (i) $x-1, y, z$; (ii) $x+1, y, z$; (iii) $-x+2, -y+1, -z+1$; (iv) $x-\frac{1}{2}, -y+\frac{1}{2}, z-\frac{1}{2}$.

the presence of two rings with orientations that define the molecular conformation (Fig. 4). In compound (3), the triazole and arene rings, bridged by an amide functionality joined through an N atom of the triazole ring, have dihedral angles between their least-squares mean planes of 53.9 (2) and 53.7 (4)°, considering the disordered A and B phenyl rings, respectively. The dihedral angle observed between those rings, separated by an amide functionality in compound (4), has a value of 29.2 (3)°. The change in the molecular conformation is a consequence of the atomic length between the rings, leaving less steric hindrance in (4), making this molecule nearly planar. In (3), a positional disorder of the arene ring is observed, which is due to a 180° rotation through the axis that contains the C10—C8 bond. This disorder was refined with occupancies of 0.42 and 0.58 for the A and B rings, respectively (Fig. 4*a*).

The conformation adopted by (**3**) is stabilized by an intramolecular hydrogen bond (N7—H1···O9; Table 4) which help to maintain the conformation observed in (3). In (4), the planar conformation allows the formation of the intramolecular hydrogen-bond interactions (N4—H1···F1 and N2—H4···O1; Table 5). The magnitude of these hydrogen-bond contacts suggests strong interactions which generate stable conformations.

The supramolecular assembly in the compounds is different and they crystallize in the space groups $P\overline{1}$ and $P2_1/n$ for (3) and (4), respectively. The different crystal packing reflects the differing molecular conformations. In the crystal structure of (3), the supramolecular assembly is directed mainly by (N,C)—H···(N,O) hydrogen-bond interactions. Initially, strong N7—H2···N6^{i} [symmetry code: (i) $-x+3, -y+1, -z+2$] hydrogen bonds form pairs of inversion-related molecules that act as slabs of infinite chains running along the [100] direction connected by a C14A—H14A···O9^{ii} [symmetry code: (ii) $x-1, y, z$] hydrogen bond (Fig. 5 and Table 5). Along the [010] direction, neighbouring chains are further connected by weak π–π interactions between two arene rings of consecutive molecules with a distance between their centroids (C10A/C15A) of 3.811 (3) Å. The supramolecular assembly in the [001] direction is maintained by dispersion and other van der Waals forces.

In compound (4), the crystal structure is built by a combination of strong N4—H1···O1^{i} and N2—H4···N3^{ii} [symmetry codes: (i) $x-1, y, z$; (ii) $x+1, y, z$] hydrogen bonds to form chains of molecules running along the [100] direction (Table 5). Parallel inversion-related chains of molecules are further connected by weaker C10—H10···O1^{iii} [symmetry code: (iii) $-x+2, -y+1, -z+1$] interactions to build the molecular

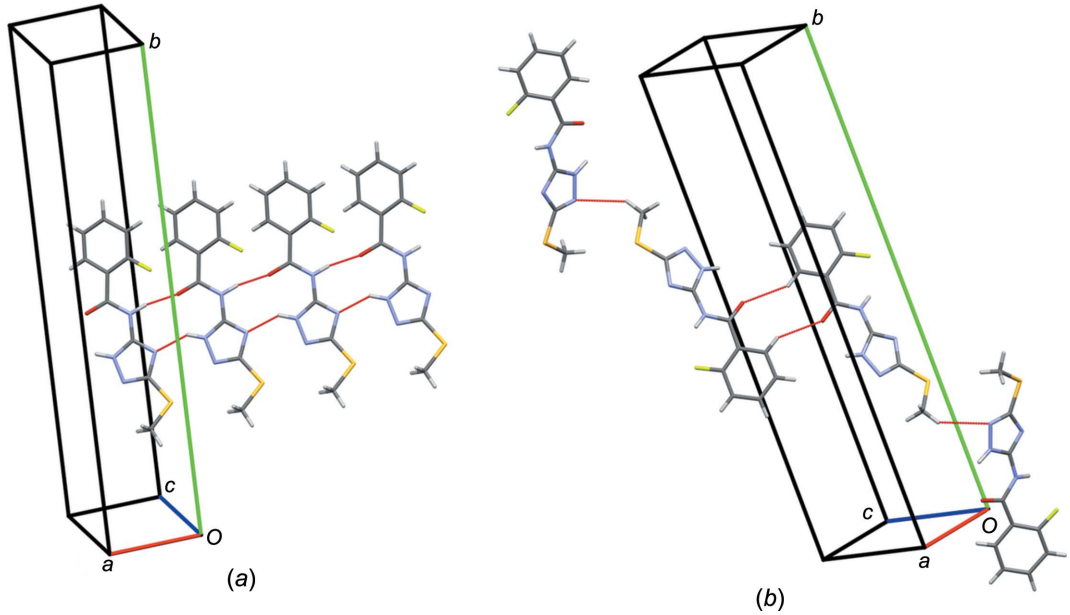

Figure 6
The crystal structure of (4), showing (*a*) the N—H···N hydrogen-bond interactions forming molecular chains along the [100] direction and (*b*) C—H···(O,N) interactions along the [001] and [010] directions.

architecture along the [001] direction. Weak C1—H1*A*···N1^{iv} [symmetry code: (iv) $x-\frac{1}{2}, -y+\frac{1}{2}, z-\frac{1}{2}$] interactions connect the molecules in order to complete the 3D structure along the [010] direction (Fig. 6).

In order to investigate these contacts further, Hirshfeld (HF) surface analysis (Turner *et al.*, 2017) mapped over d_{norm} (analysis of the contact distances d_i and d_e from the HF surface to the nearest atom inside and outside, respectively) was performed. The results reveal that in (3), the N7—H2···N6^{i} and C14*A*—H14*A*···O9^{ii} hydrogen bonds, observed as bright-red spots over d_{norm}, are the most important interactions to build the supramolecular assembly (Figs. 7*a* and 7*b*), with H···N/N···H and H···O/O···H contacts comprising 15.4 and 5.0%, respectively, of the total HF surface, as observed in the two-dimensional (2D) fingerplots (see supporting information). The weak π–π stacking and C—H···π interactions are corroborated in the HF surface by the observation of red spots of low intensity over the arene ring. In this case, C···C contacts have a low contribution to the HF surface, with a value of 2.5%, as expected. The 2D fingerprint plots reveal the existence of other contributions to the crystal structure, such as H···S/S···H (10.9%) and H···F/F···H (7.8%) contacts which are the result of weak C13—H13···S1 interactions and the probable contact between the H atoms of the methylsulfanyl group and the F atom of the arene ring. These interactions were not observed previously due to their weakness, with lengths that surpasses the values (~2.9 Å) expected for a contact of considerable importance. Despite the low intensity of the red spot on the HF surface, there is another contact that is observable over d_{norm}. This is a C···F interaction between the carbonyl group and the F atom of the disordered arene ring of two adjacent molecules (Fig. 7*b*). The contact would be the result of the polarization of the carbonyl group, leaving the C atom with a positive partial charge which, in fact, interacts with the F atom. In the formation of the crystal structure, van der Waals forces seem to play an important role, which is observed in the H···C/C···H (16.9%) and nonbonded H···H (27.3%) contacts.

Table 6
CE–HF interaction energies (kJ mol^{-1}; 1 kJ mol^{-1} = 0.239 kcal mol^{-1}) for (3).

N is the number of molecules with an *R* molecular centroid-to-centroid distance (Å). Electron density was calculated using HF/3-21G model energies.

N	*R*	E_{ele}	E_{pol}	E_{dis}	E_{rep}	E_{tot}*
1	8.38	−144.9	−3.8	−19.7	8.9	−160.6
1	5.48	−234.2	−13.6	−72.5	18.6	−297.7
1	5.89	−181.1	−89.3	−142.9	85.5	−302.1
1	11.13	−100.3	−0.3	−2.5	0.0	−104.6
2	10.01	−105.2	−8.6	−20.3	4.7	−127.3
2	10.48	−124.0	−6.3	−12.6	16.7	−128.3
1	7.66	−153.2	−8.1	−42.0	20.0	−183.0
2	7.66	−149.0	−8.6	−27.8	49.6	−142.3
1	5.55	−242.6	−25.3	−67.1	19.7	−308.2
1	7.16	−192.1	−9.1	−34.6	−1.2	−233.7
1	10.32	−189.7	−27.0	−16.7	58.5	−178.5

Note: (*) scale factors used to determine E_{tot}: E_{ele} = 1.019, E_{pol} = 0.651, E_{dis} = 0.901 and E_{rep} = 0.811.

The electrostatic potential for (3) was calculated using *TONTO* (Fig. 7*c*), a Fortran-based object-oriented system for quantum chemistry and crystallography (Spackman *et al.*, 2008; Jayatilaka *et al.*, 2005; *TONTO* is available at hirshfeldsurface.net), and subsequently mapped over the HF surface using the STO-3G basis set at the Hartree–Fock level of theory over the range of ±0.14 a.u. The discussed contacts

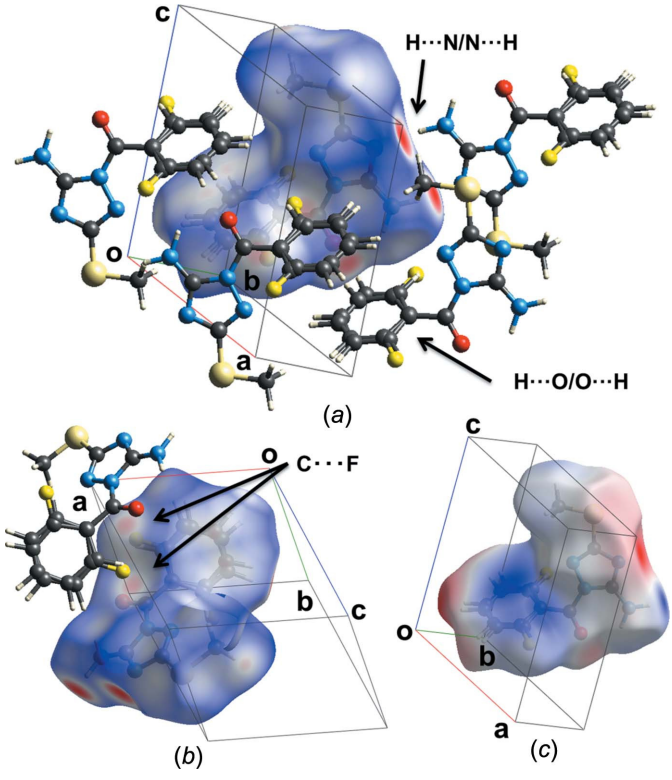

Figure 7
A view of the Hirshfeld surfaces mapped over (*a*)/(*b*) d_{norm}, emphasizing the intermolecular interactions H···N/N···H, H···O/O···H and C···F, and (*c*) the electrostatic potential with positive and negative potential indicated in blue and red, respectively.

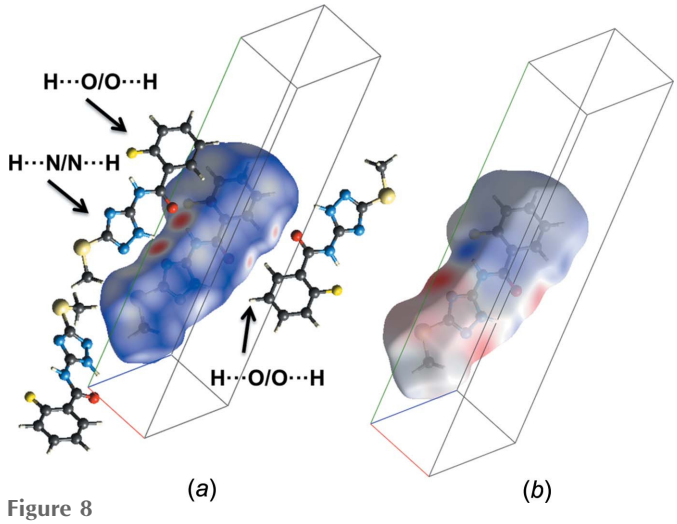

Figure 8
A view of the Hirshfeld surfaces mapped over (*a*) d_{norm}, emphasizing the intermolecular interactions H···N/N···H, H···O/O···H, and (*b*) the electrostatic potential with positive and negative potential indicated in blue and red, respectively.

Table 7
CE–HF interaction energies (kJ mol^{-1}; 1 kJ mol^{-1} = 0.239 kcal mol^{-1}) for (4).

N is the number of molecules with an *R* molecular centroid-to-centroid distance (Å). Electron density was calculated using HF/3-21G model energies.

N	*R*	E_{ele}	E_{pol}	E_{dis}	E_{rep}	E_{tot}*
1	5.97	−22.5	−5.0	−21.2	6.7	−39.9
2	5.05	−45.2	−15.1	−39.2	47.1	−53.1
2	11.19	−1.4	−1.3	−9.9	4.5	−7.5
2	11.32	−1.4	−1.0	−6.4	3.8	−4.8
2	13.52	−6.2	−1.4	−7.6	5.4	−9.7
1	4.29	−8.1	−3.0	−62.6	24.3	−46.8
2	13.72	−1.0	−0.7	−5.8	2.2	−4.8
1	6.03	−10.2	−3.2	−42.4	16.0	−37.8
1	8.03	−12.8	−3.3	−15.9	8.7	−22.5

Note: (*) scale factors used to determine E_{tot}: E_{ele} = 1.019, E_{pol} = 0.651, E_{dis} = 0.901 and E_{rep} = 0.811.

observed over d_{norm} were corroborated by the hydrogen-bond donor region with positive potential (blue region) and the acceptor region with negative potential (red region).

HF surface analysis mapped over d_{norm} was also performed for compound (4). As observed in the 2D fingerprint plots (see supporting information), the bright-red spots (Fig. 8*a*) referring to H···N/N···H and H···O/O···H contacts comprise 15.5 and 7.0% of the total HF surface, respectively, leaving these interactions as the most important, in terms of strength, in the building of the crystal structure. C10—H10···O1^{iii} interactions, represented by less bright spots, also play an important role in the supramolecular assembly, with H···O/O···H contacts comprising 7.0% of the surface. A closer observation of the HF surface allows the imagining of another sort of weak interactions involved in the formation of the crystal, presumably dispersion and other van de Waals forces, detected in the H···C/C···H and nonbonded H···H contacts, with values of 11.0 and 30.6%, respectively. The higher value of the nonbonded contacts in (4) is consistent with the few closer contacts, which indicates an absence of strong connections around the blue region (Fig. 8*a*). In this region, only long-range hydrophobic interactions are present, which suggests a considerable hydrophobicity in the formation of the crystal. This observation is consistent with the fact that compounds (3) and (4) are soluble in chloroform and dimethyl sulfoxide, respectively. The HF analysis also suggests interactions such as H···S/S···H (11.9%) and H···F/F···H (3.9%). However, these contacts are not observed clearly in the HF surface, unlike in the case of compound (3). In (4), there is a low contribution from C···C contacts (5.1%) as a result of the low contribution from C—H···π and π–π stacking interactions. The electrostatic potential mapped over the HF surface corroborates the hydrogen-bond donor regions with positive potential (blue cloud) and the acceptor regions with negative potential (red cloud) (Fig. 8*b*).

The crystallographic architectures described for (3) and (4) are based mainly on short contacts. In order to describe these interactions as a whole-of-molecule approach and not as specific atom–atom contacts, energy models of the interactions between molecules in the construction of the crystals were analyzed. These interactions were calculated using the HF/3-21G energy model implemented in *CrystalExplorer* (CE; Turner *et al.*, 2017), which uses quantum mechanical charge distributions for unperturbed molecules (Mackenzie *et al.*, 2017). In these calculations, the total interaction energy is modelled as the sum of the electrostatic (E_{ele}), polarization (E_{pol}), dispersion (E_{dis}) and exchange–repulsion (E_{rep}) terms (Mackenzie *et al.*, 2017). In Table 6, the interaction energies for selected molecular pairs in the first coordination sphere around the asymmetric unit for compound (3) are summarized. Observing the results, it is possible to deduce that the electrostatic term contributes the greatest proportion to the total energy in all the possible interactions of the asymmetric unit with neighbouring molecules. This 3D distribution of

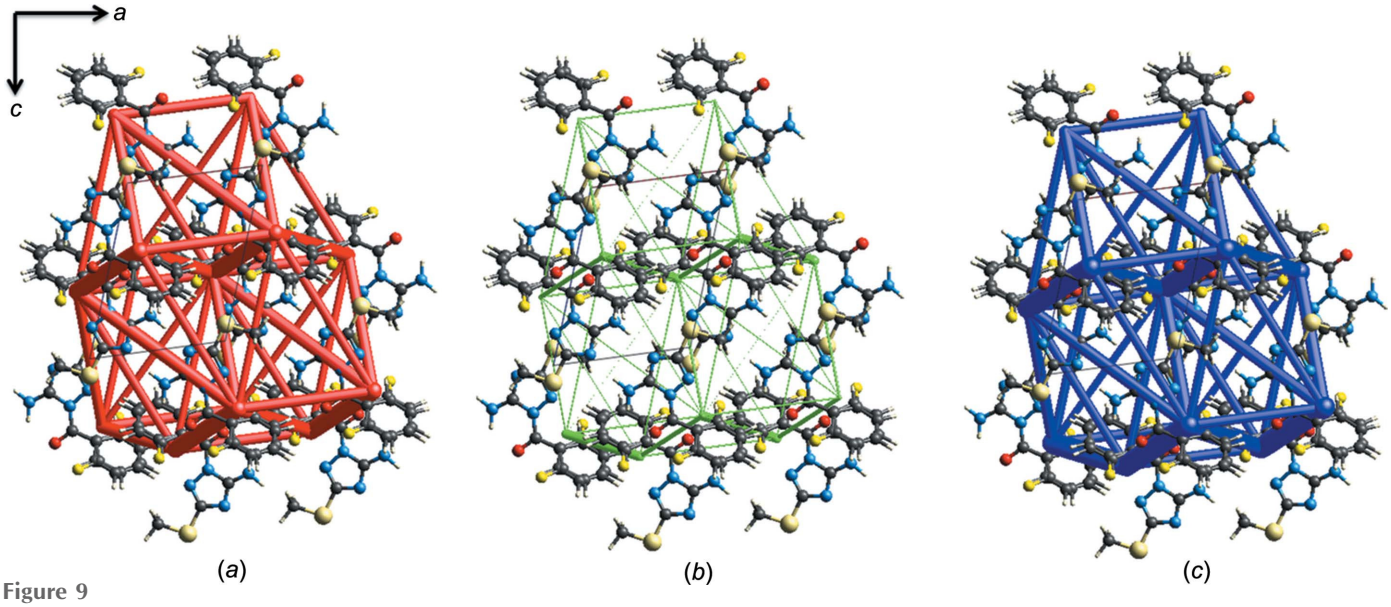

Figure 9
Energy-framework diagrams for (*a*) electrostatic (red) and (*b*) dispersion (green) contributions to (*c*) the total interaction energies (blue) in compound (3).

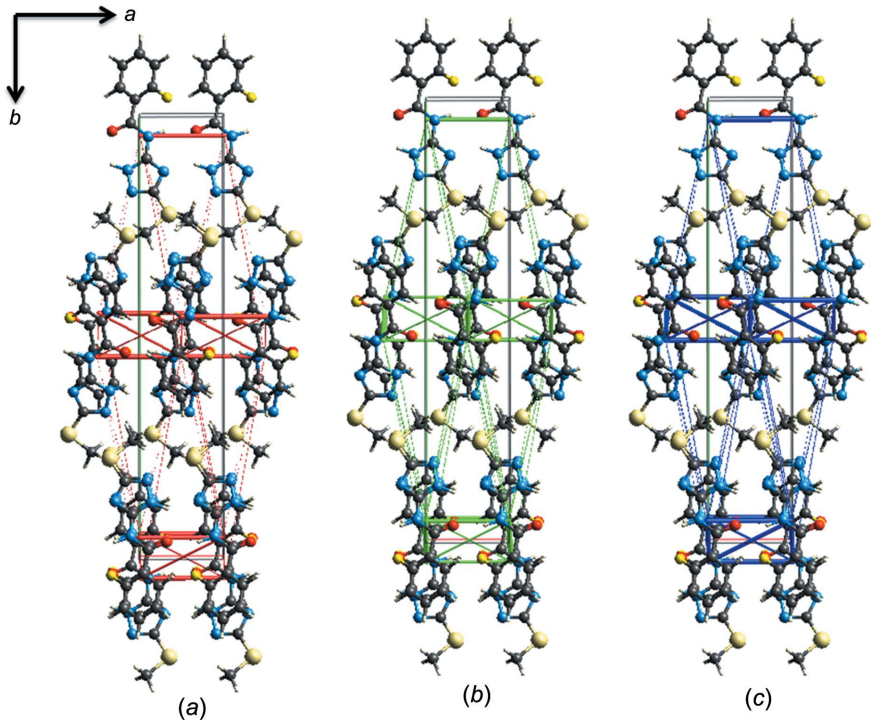

Figure 10
Energy-framework diagrams for (*a*) electrostatic (red) and (*b*) dispersion (green) contributions to (*c*) the total interaction energies (blue) in compound (4).

electrostatic energies shows that there are strong interactions in all directions between the molecules that form the crystal, which results in complementary information with respect to the atom–atom analysis. The molecules connected by strong N7—H2···N6^{i} and C14*A*—H14*A*···O9^{ii} hydrogen bonds have total energy values of −55.9 and −34.0 kcal mol^{-1}, respectively. The dispersion and polarization terms contribute less to the formation of the crystal, except for the observed π–π interactions between two arene rings of consecutive molecules with dispersion and polarization energy values of 34.2 and −21.3 kcal mol^{-1}, respectively. Fig. 9 shows the energy framework diagrams for pairs of molecules for separate, electrostatic (red) and dispersion (green) contributions to the total nearest-neighbour pairwise interaction energies (blue). As observed, the cylinders help as a guide that connects molecular centroids and their respective thicknesses represent the relative magnitude of the energy. It is important to notice that the principal force that constructs the crystal corresponds to the electrostatic energy.

The total interaction energy was modeled for (4) and the results are summarized in Table 7. The strongest pairwise interaction, with a total energy value of −53.1 kJ mol^{-1}, corresponds to the combination of strong N4—H1···O1^{i} and N2—H4···N3^{ii} hydrogen bonds. In this case, the electrostatic term contributes mainly to this interaction. The second highest value of the total energy, −46.8 kJ mol^{-1}, corresponds to an intermolecular interaction represented mainly by the dispersion term (−62.6 kJ mol^{-1}) involving van der Waals forces between two nearly parallel molecules, an important interaction not seen before. Fig. 10, showing the energy framework diagrams for pairs of molecules, suggests a nearly equivalent contribution from the electrostatic and dispersion terms to the total energy, which in fact seems to be more anisotropic than that observed in compound (3). The electrostatic term is oriented along the [100] direction connecting the N atoms of the exocyclic amine groups of neighbouring molecules, differing from the 3D distribution observed in compound (3). Along the [010] and [001] directions, the electrostatic energy is rather weak. The dispersion term has a 2D character connecting molecules preferentially to form (001) sheets. The different distribution of the electrostatic and dispersion terms to the total energy in molecules with structural similarities was also observed in other 4-aryl-2-methyl-1*H*-imidazoles (Macías *et al.*, 2018*b*).

Acknowledgements

We thank Professor Jaime Portilla (Universidad de los Andes) for providing access to microwave equipment and Edwin Guevara (Universidad de los Andes) for acquiring the mass spectra. We also acknowledge Professor Rodrigo Abonía (Universidad del Valle) for his valuable contribution to the discussion of this work.

Funding information

Funding for this research was provided by: Universidad del Valle, Colombia (project number CI-1129 to RMF).

References

Abdel-Megeed, A. M., Abdel-Rahman, H. M., Alkaramany, G.-E. & El-Gendy, M. A. (2009). *Eur. J. Med. Chem.* **44**, 117–123.

Acosta, P., Becerra, D., Goudedranche, S., Quiroga, J., Constantieux, T., Bonne, D. & Rodriguez, J. (2015). *Synlett*, **26**, 1591–1595.

Aggarwal, N., Kumar, R., Dureja, P. & Khurana, J. M. (2011). *Eur. J. Med. Chem.* **46**, 4089–4099.

Agilent (2014). *CrysAlis PRO*. Agilent Technologies Ltd, Yarnton, Oxfordshire, England.

Almasirad, A., Tabatabai, S. A., Faizi, M., Kebriaeezadeh, A., Mehrabi, N., Dalvandi, A. & Shafiee, A. (2004). *Bioorg. Med. Chem. Lett.* **14**, 6057–6059.

Aneja, B., Azam, M., Alam, S., Perwez, A., Maguire, R., Yadava, U., Kavanagh, K., Daniliuc, C. G., Rizvi, M. M. A., Haq, Q. M. R. & Abid, M. (2018). *ACS Omega*, **3**, 6912–6930.

Balkus, K. J., Khanmamedova, A. K. & Woo, R. (1998). *J. Mol. Catal. A Chem.* **134**, 137–143.

Becke, A. D. (1993). *J. Chem. Phys.* **98**, 5648–5652.

Castillo, J.-C., Jiménez, E., Portilla, J., Insuasty, B., Quiroga, J., Moreno-Fuquen, R., Kennedy, A. R. & Abonia, R. (2018*a*). *Tetrahedron*, **74**, 932–947.

Castillo, J.-C., Tigreros, A. & Portilla, J. (2018*b*). *J. Org. Chem.* **83**, 10887–10897.

Chohan, Z. H. & Hanif, M. (2013). *J. Enzyme Inhib. Med. Chem.* **28**, 944–953.

Chouke, P. B. & Ingle, V. N. (2012). *Der Pharma Chem*. **4**, 377–382.

Connolly, P. J., Emanuel, S., Gruninger, R. H., Huang, S., Lin, R., Middleton, S. A. & Wetter, S. K. (2006). Patent No. WO2006042215 A1.

Dolzhenko, A. V., Dolzhenko, A. V. & Chui, W.-K. (2006). *Heterocycles*, **68**, 1723–1759.

Dolzhenko, A. V., Pastorin, G., Dolzhenko, A. V. & Chui, W. K. (2009). *Tetrahedron Lett.* **50**, 2124–2128.

Dżygiel, A., Masiukiewicz, E. & Rzeszotarska, B. (2002). *J. Agric. Food Chem.* **50**, 1383–1388.

El-Husseiny, W. M., El-Sayed, M. A.-A., Abdel-Aziz, N. I., El-Azab, A. S., Asiri, Y. A. & Abdel-Aziz, A. A. (2018). *Eur. J. Med. Chem.* **158**, 134–143.

Ferrini, S., Ponticelli, F. & Taddei, M. (2007). *Org. Lett.* **9**, 69–72.

Fidler, Z. N., Shibanova, E. F., Makerov, P. V., Kalikhman, I. D., Shulunova, A. M., Sarapulova, G. I., Klyba, L. V., Vitkovskii, V. Y., Chipanina, N. N., Lopyrev, V. A. & Voronkov, M. G. (1980). *Chem. Heterocycl. Compd.* **16**, 1079–1083.

Fischer, G. (2008). *Adv. Heterocycl. Chem.* **95**, 143–219.

Frisch, M. J., *et al.* (2009). *GAUSSIAN09*. Revision A.02. Gaussian Inc., Wallingford, CT, USA. http://www.gaussian.com.

Giroud, M., Kuhn, B., Saint-Auret, S., Kuratli, C., Martin, R. E., Schuler, F., Diederich, F., Kaiser, M., Brun, R., Schirmeister, T. & Haap, W. (2018). *J. Med. Chem.* **61**, 3370–3388.

Häring, M., Rodríguez-López, J., Grijalvo, S., Tautz, M., Eritja, R., Martín, V. S. & Díaz Díaz, D. (2018). *Mol. Pharm.* **15**, 2963–2972.

Hassan, A. Y., Sarg, M. T., Bayoumi, A. H. & El-Deeb, M. A. (2018). *J. Heterocycl. Chem.* **55**, 1450–1478.

Hohenberg, P. & Kohn, W. (1964). *Phys. Rev.* **136**, B864–B871.

Insuasty, B., Becerra, D., Quiroga, J., Abonia, R., Nogueras, M. & Cobo, J. (2013). *Eur. J. Med. Chem.* **60**, 1–9.

Jagdish, K. S., Swastika, G. & Atul, K. (2013). *Chin. J. Nat. Med.* **11**, 456–465.

Jayatilaka, D., Grimwood, D. J., Lee, A., Lemay, A., Russel, A. J., Taylor, C., Wolff, S. K., Cassam-Chenai, P. & Whitton, A. (2005). *TONTO*. http://hirshfeldsurface.net/.

Kantheti, S., Narayan, R. & Raju, K. V. S. N. (2015). *RSC Adv.* **5**, 3687–3708.

Kappe, C. O. (2008). *Chem. Soc. Rev.* **37**, 1127–1139.

Karpińska, G. & Dobrowolski, J. C. (2008). *J. Mol. Struct. Theochem*, **853**, 7–17.

Khalil, N. S. A. M. (2006). *Carbohydr. Res.* **341**, 2187–2199.

Krause, T., Baader, S., Erb, B. & Goossen, L. J. (2016). *Nat. Commun.* **7**, 11732–11739.

Lee, C., Yang, W. & Parr, R. G. (1988). *Phys. Rev. B*, **37**, 785–789.

Liebeskind, L. S. & Srogl, J. (2002). *Org. Lett.* **4**, 979–981.

Macías, M. A., Castillo, J.-C. & Portilla, J. (2018*a*). *Acta Cryst.* C**74**, 82–93.

Macías, M. A., Elejalde, N.-R., Butassi, E., Zacchino, S. & Portilla, J. (2018*b*). *Acta Cryst.* C**74**, 1447–1458.

Mackenzie, C. F., Spackman, P. R., Jayatilaka, D. & Spackman, M. A. (2017). *IUCrJ*, **4**, 575–587.

Macrae, C. F., Bruno, I. J., Chisholm, J. A., Edgington, P. R., McCabe, P., Pidcock, E., Rodriguez-Monge, L., Taylor, R., van de Streek, J. & Wood, P. A. (2008). *J. Appl. Cryst.* **41**, 466–470.

Martins, M. A. P., Paveglio, G. C., Munchen, T. S., Meyer, A. R., Moreira, D. N., Rodrigues, L. V., Frizzo, C. P., Zanatta, N., Bonacorso, H. G., Melo, P. A. & Krzyzaniak, S. R. (2016). *J. Mol. Liq.* **223**, 934–938.

Moghaddam, F. M., Ghaffarzadeh, M. & Abdi-Oskoui, S. H. (1999). *J. Chem. Res.* pp. 574–575.

Moreno-Fuquen, R., Castillo, J. C., Becerra, D., Camargo, H. & Henao, J. A. (2015). *Acta Cryst.* E**71**, o882–o883.

Moreno-Fuquen, R., Cuenú, F., Torres, J. E., De la Vega, G., Galarza, E., Abonia, R. & Kennedy, A. R. (2017). *J. Mol. Struct.* **1150**, 366–373.

Moreno-Fuquen, R., Sánchez, D. F. & Ellena, J. (2014). *Acta Cryst.* E**70**, o1252.

Nocentini, A., Ferraroni, M., Carta, F., Ceruso, M., Gratteri, P., Lanzi, C., Masini, E. & Supuran, C. T. (2016). *J. Med. Chem.* **59**, 10692–10704.

Ojeda-Porras, A. & Gamba-Sánchez, D. (2016). *J. Org. Chem.* **81**, 11548–11555.

Ozimiński, W. P., Dobrowolski, J. C. & Mazurek, A. P. (2004). *J. Mol. Struct. Theochem*, **680**, 107–115.

Palatinus, L. & Chapuis, G. (2007). *J. Appl. Cryst.* **40**, 786–790.

Palmer, M. H. & Christen, D. (2004). *J. Mol. Struct.* **705**, 177–187.

Reiter, J., Pongó, L. & Dvortsák, P. (1987). *J. Heterocycl. Chem.* **24**, 127–142.

Sheldrick, G. M. (2015). *Acta Cryst.* C**71**, 3–8.

Shibl, M. F., Elroby, S. A. K. & Hilal, R. H. (2011). *Mol. Simul.* **37**, 11–17.

Singh, N. & Dureja, P. (2000). *J. Environ. Sci. Health B*, **35**, 549–558.

Singh, R., Sylvain, C., Holland, S., Zhang, J., Partridge, J. J. & Clough, J. (2007). Patent No. WO2007030680 A3.

Somorai, T., Szilágyi, G., Reiter, J., Pongó, L., Láng, T., Toldy, L. & Horváth, S. (1986). *Arch. Pharm.* **319**, 238–242.

Sorescu, D. C., Bennett, C. M. & Thompson, D. L. (1998). *J. Phys. Chem. A*, **102**, 10348–10357.

Spackman, M. A., McKinnon, J. J. & Jayatilaka, D. (2008). *CrystEngComm*, **10**, 377–388.

Trinh, M. N., Lu, F., Li, X., Das, A., Liang, Q., De Brabander, J. K., Brown, M. S. & Goldstein, J. L. (2017). *Proc. Natl Acad. Sci. USA*, **114**, 89–94.

Turner, M. J., McKinnon, J. J., Wolff, S. K., Grimwood, D. J., Spackman, P. R., Jayatilaka, D. & Spackman, M. A. (2017). *CrystalExplorer17*. University of Western Australia. http://hirshfeldsurface.net/.

Viana, R. B., Ribeiro, G. L. O., Santos, S. F. F., Quintero, D. E., Viana, A. B., da Silva, A. B. F. & Moreno-Fuquen, R. (2016). *Spectrochim. Acta A Mol. Biomol. Spectrosc.* **162**, 16–26.

Yu, S., Chai, X., Wang, Y., Cao, Y., Zhang, J., Wu, Q., Zhang, D., Jiang, Y., Yan, T. & Sun, Q. (2014). *Drug. Des. Dev. Ther.* pp. 383–390.

supporting information

Acta Cryst. (2019). C**75**, 359-371 [https://doi.org/10.1107/S2053229619002572]

Catalyst- and solvent-free synthesis of 2-fluoro-*N*-(3-methylsulfanyl-1*H*-1,2,4-triazol-5-yl)benzamide through a microwave-assisted Fries rearrangement: X-ray structural and theoretical studies

Rodolfo Moreno-Fuquen, Kevin Arango-Daraviña, Diana Becerra, Juan-Carlos Castillo, Alan R. Kennedy and Mario A. Macías

Computing details

For both structures, data collection: *CrysAlis PRO* (Agilent, 2014); cell refinement: *CrysAlis PRO* (Agilent, 2014); data reduction: *CrysAlis PRO* (Agilent, 2014); program(s) used to solve structure: SUPERFLIP (Palatinus & Chapuis, 2007); program(s) used to refine structure: *SHELXL2014* (Sheldrick, 2015); molecular graphics: *Mercury* (Macrae *et al.*, 2008); software used to prepare material for publication: *SHELXL2014* (Sheldrick, 2015).

(5-Amino-3-methylsulfanyl-1*H*-1,2,4-triazol-1-yl)(2-fluorophenyl)methanon (Compound_3)

Crystal data

$C_{10}H_9FN_4OS$
$M_r = 252.27$
Triclinic, $P\overline{1}$
$a = 7.6599$ (9) Å
$b = 7.8079$ (8) Å
$c = 10.0140$ (12) Å
$\alpha = 94.487$ (9)°
$\beta = 108.668$ (11)°
$\gamma = 97.565$ (9)°
$V = 557.83$ (12) Å^3
$Z = 2$
$F(000) = 260$
$D_x = 1.502$ Mg m^{-3}
Mo $K\alpha$ radiation, $\lambda = 0.71073$ Å
Cell parameters from 5358 reflections
$\theta = 3.6$–27.5°
$\mu = 0.29$ mm^{-1}
$T = 298$ K
Parallelepiped, colorless
0.38 × 0.34 × 0.22 mm

Data collection

Agilent SuperNova Dual Source diffractometer with an Atlas detector′
Radiation source: SuperNova (Mo) X-ray Source
Detector resolution: 5.3072 pixels mm^{-1}
ω scans
Absorption correction: multi-scan (CrysAlis PRO; Agilent, 2014)
$T_{min} = 0.856$, $T_{max} = 1.000$
12256 measured reflections
2450 independent reflections
2107 reflections with $I > 2\sigma(I)$
$R_{int} = 0.044$
$\theta_{max} = 27.1°$, $\theta_{min} = 2.9°$
$h = -9 \rightarrow 9$
$k = -9 \rightarrow 10$
$l = -12 \rightarrow 12$

Refinement

Refinement on F^2
Least-squares matrix: full
$R[F^2 > 2\sigma(F^2)] = 0.042$
$wR(F^2) = 0.116$
$S = 0.89$
2450 reflections
225 parameters
159 restraints

Primary atom site location: iterative
Secondary atom site location: difference Fourier map
Hydrogen site location: mixed
H atoms treated by a mixture of independent and constrained refinement

$w = 1/[\sigma^2(F_o^2) + (0.0563P)^2 + 0.4216P]$ where $P = (F_o^2 + 2F_c^2)/3$
$(\Delta/\sigma)_{max} = 0.001$
$\Delta\rho_{max} = 0.27$ e Å^{-3}
$\Delta\rho_{min} = -0.22$ e Å^{-3}

Special details

Geometry. All esds (except the esd in the dihedral angle between two l.s. planes) are estimated using the full covariance matrix. The cell esds are taken into account individually in the estimation of esds in distances, angles and torsion angles; correlations between esds in cell parameters are only used when they are defined by crystal symmetry. An approximate (isotropic) treatment of cell esds is used for estimating esds involving l.s. planes.

Fractional atomic coordinates and isotropic or equivalent isotropic displacement parameters (Å²)

	x	*y*	*z*	U_{iso}*/U_{eq}	Occ. (<1)
S1	1.02515 (8)	0.25941 (8)	1.09852 (5)	0.05278 (19)	
H1	1.373 (3)	0.476 (3)	0.7053 (6)	0.063*	
H2	1.4957 (16)	0.518 (3)	0.8587 (18)	0.063*	
C10A	0.8191 (3)	0.2346 (10)	0.5115 (8)	0.0367 (4)	0.633 (3)
C11A	0.7667 (7)	0.1073 (11)	0.3944 (7)	0.0377 (5)	0.633 (3)
C12A	0.5846 (5)	0.0481 (9)	0.3128 (7)	0.0465 (12)	0.633 (3)
H12A	0.554375	−0.037357	0.235294	0.056*	0.633 (3)
C13A	0.4464 (5)	0.1184 (5)	0.3483 (4)	0.0399 (5)	0.633 (3)
H13A	0.321606	0.079988	0.294066	0.048*	0.633 (3)
C14A	0.4925 (5)	0.2463 (5)	0.4645 (4)	0.0391 (4)	0.633 (3)
H14A	0.399095	0.295157	0.486343	0.047*	0.633 (3)
C15A	0.6781 (2)	0.3005 (7)	0.5474 (5)	0.0380 (4)	0.633 (3)
H15A	0.708397	0.381670	0.627779	0.046*	0.633 (3)
F1A	0.9121 (3)	0.0504 (3)	0.3615 (2)	0.0532 (6)	0.633 (3)
C10B	0.8175 (4)	0.2377 (16)	0.5144 (14)	0.0371 (4)	0.367 (3)
C11B	0.7981 (9)	0.1168 (17)	0.3994 (10)	0.0371 (16)	0.367 (3)
H11B	0.903845	0.091889	0.380400	0.045*	0.367 (3)
C12B	0.6220 (13)	0.0324 (17)	0.3122 (13)	0.0390 (5)	0.367 (3)
H12B	0.612361	−0.055916	0.241001	0.047*	0.367 (3)
C13B	0.4644 (11)	0.0767 (9)	0.3292 (7)	0.0394 (5)	0.367 (3)
H13B	0.347918	0.018856	0.269960	0.047*	0.367 (3)
C14B	0.4765 (9)	0.2065 (9)	0.4335 (7)	0.0389 (4)	0.367 (3)
H14B	0.368949	0.241264	0.442838	0.047*	0.367 (3)
C15B	0.6519 (3)	0.2856 (12)	0.5254 (8)	0.0380 (4)	0.367 (3)
F1B	0.6863 (5)	0.4163 (5)	0.6360 (4)	0.0557 (11)	0.367 (3)
N3	0.9653 (2)	0.2605 (2)	0.81764 (16)	0.0400 (4)	
N4	1.0763 (2)	0.3271 (2)	0.74015 (16)	0.0392 (4)	
C5	1.2529 (3)	0.3998 (3)	0.8343 (2)	0.0426 (4)	
N6	1.2581 (2)	0.3836 (2)	0.96490 (18)	0.0466 (4)	
N7	1.3908 (3)	0.4744 (3)	0.7944 (2)	0.0603 (5)	
C2	1.0807 (3)	0.3004 (3)	0.9475 (2)	0.0412 (4)	
C8	1.01785 (18)	0.3102 (2)	0.59287 (17)	0.0372 (4)	
O9	1.12866 (18)	0.3549 (2)	0.53342 (15)	0.0490 (4)	

C18	0.7830 (3)	0.1643 (3)	1.0186 (2)	0.0593 (6)
H18A	0.724733	0.160853	1.090360	0.089*
H18B	0.773136	0.047986	0.974666	0.089*
H18C	0.721750	0.233088	0.948057	0.089*

Atomic displacement parameters (Å²)

	U^{11}	U^{22}	U^{33}	U^{12}	U^{13}	U^{23}
S1	0.0504 (3)	0.0689 (4)	0.0336 (3)	0.0007 (3)	0.0098 (2)	0.0081 (2)
C10A	0.0323 (6)	0.0437 (8)	0.0337 (8)	0.0040 (6)	0.0108 (6)	0.0064 (6)
C11A	0.0327 (8)	0.0447 (10)	0.0346 (9)	0.0044 (8)	0.0107 (7)	0.0053 (7)
C12A	0.033 (2)	0.062 (3)	0.0362 (16)	0.004 (2)	0.002 (2)	0.0024 (16)
C13A	0.0332 (7)	0.0470 (10)	0.0367 (9)	0.0049 (7)	0.0090 (7)	0.0031 (7)
C14A	0.0328 (6)	0.0465 (9)	0.0360 (9)	0.0044 (7)	0.0100 (6)	0.0037 (7)
C15A	0.0325 (6)	0.0454 (9)	0.0348 (9)	0.0039 (6)	0.0104 (6)	0.0048 (7)
F1A	0.0518 (12)	0.0632 (13)	0.0447 (11)	0.0182 (9)	0.0155 (9)	−0.0049 (9)
C10B	0.0324 (7)	0.0441 (9)	0.0340 (8)	0.0040 (7)	0.0107 (6)	0.0060 (7)
C11B	0.021 (3)	0.054 (4)	0.034 (3)	−0.001 (3)	0.008 (3)	0.009 (2)
C12B	0.0329 (8)	0.0462 (10)	0.0358 (10)	0.0049 (8)	0.0098 (8)	0.0038 (8)
C13B	0.0331 (7)	0.0466 (10)	0.0362 (9)	0.0049 (7)	0.0095 (7)	0.0030 (8)
C14B	0.0327 (6)	0.0462 (10)	0.0358 (9)	0.0044 (7)	0.0100 (6)	0.0035 (7)
C15B	0.0326 (6)	0.0453 (9)	0.0348 (9)	0.0041 (7)	0.0104 (6)	0.0047 (7)
F1B	0.056 (2)	0.062 (2)	0.054 (2)	0.0153 (16)	0.0248 (16)	−0.0005 (16)
N3	0.0366 (8)	0.0471 (9)	0.0338 (8)	−0.0019 (6)	0.0119 (6)	0.0042 (6)
N4	0.0319 (8)	0.0479 (9)	0.0339 (8)	−0.0032 (6)	0.0103 (6)	0.0012 (6)
C5	0.0322 (9)	0.0475 (11)	0.0418 (10)	−0.0003 (8)	0.0077 (8)	0.0003 (8)
N6	0.0355 (8)	0.0572 (10)	0.0396 (9)	−0.0008 (7)	0.0065 (7)	0.0021 (7)
N7	0.0349 (9)	0.0893 (15)	0.0445 (10)	−0.0158 (9)	0.0088 (8)	0.0000 (10)
C2	0.0362 (9)	0.0458 (10)	0.0377 (10)	0.0021 (8)	0.0090 (8)	0.0047 (8)
C8	0.0342 (9)	0.0409 (9)	0.0375 (9)	0.0054 (7)	0.0137 (7)	0.0050 (7)
O9	0.0373 (7)	0.0676 (10)	0.0435 (8)	0.0012 (6)	0.0184 (6)	0.0064 (7)
C18	0.0531 (13)	0.0743 (16)	0.0490 (12)	−0.0062 (11)	0.0220 (10)	0.0059 (11)

Geometric parameters (Å, º)

S1—C2	1.739 (2)	C12B—H12B	0.9300
S1—C18	1.796 (2)	C13B—C14B	1.369 (7)
C10A—C15A	1.388 (5)	C13B—H13B	0.9300
C10A—C11A	1.391 (5)	C14B—C15B	1.391 (6)
C10A—C8	1.491 (2)	C14B—H14B	0.9300
C11A—C12A	1.367 (6)	C15B—F1B	1.380 (8)
C11A—F1A	1.374 (6)	N3—C2	1.303 (2)
C12A—C13A	1.382 (5)	N3—N4	1.402 (2)
C12A—H12A	0.9300	N4—C8	1.387 (2)
C13A—C14A	1.392 (4)	N4—C5	1.393 (2)
C13A—H13A	0.9300	C5—N6	1.312 (3)
C14A—C15A	1.386 (4)	C5—N7	1.326 (3)
C14A—H14A	0.9300	N6—C2	1.377 (2)

C15A—H15A	0.9300	N7—H1	0.8600 (11)
C10B—C11B	1.386 (9)	N7—H2	0.8600 (11)
C10B—C15B	1.403 (7)	C8—O9	1.214 (2)
C10B—C8	1.491 (2)	C18—H18A	0.9600
C11B—C12B	1.392 (10)	C18—H18B	0.9600
C11B—H11B	0.9300	C18—H18C	0.9600
C12B—C13B	1.356 (9)		

C2—S1—C18	100.21 (10)	C13B—C14B—C15B	119.0 (6)
C15A—C10A—C11A	117.7 (3)	C13B—C14B—H14B	120.5
C15A—C10A—C8	119.2 (3)	C15B—C14B—H14B	120.5
C11A—C10A—C8	123.0 (4)	F1B—C15B—C14B	125.7 (4)
C12A—C11A—F1A	121.8 (4)	F1B—C15B—C10B	112.1 (4)
C12A—C11A—C10A	123.0 (5)	C14B—C15B—C10B	122.2 (6)
F1A—C11A—C10A	115.2 (3)	C2—N3—N4	101.36 (14)
C11A—C12A—C13A	118.4 (5)	C8—N4—C5	127.12 (15)
C11A—C12A—H12A	120.8	C8—N4—N3	123.84 (14)
C13A—C12A—H12A	120.8	C5—N4—N3	108.91 (15)
C12A—C13A—C14A	120.5 (4)	N6—C5—N7	126.71 (18)
C12A—C13A—H13A	119.7	N6—C5—N4	109.42 (16)
C14A—C13A—H13A	119.7	N7—C5—N4	123.86 (18)
C15A—C14A—C13A	119.8 (3)	C5—N6—C2	103.34 (16)
C15A—C14A—H14A	120.1	C5—N7—H1	119.0 (17)
C13A—C14A—H14A	120.1	C5—N7—H2	118.8 (17)
C14A—C15A—C10A	120.5 (3)	H1—N7—H2	122 (2)
C14A—C15A—H15A	119.7	N3—C2—N6	116.95 (17)
C10A—C15A—H15A	119.7	N3—C2—S1	124.73 (15)
C11B—C10B—C15B	116.3 (5)	N6—C2—S1	118.31 (14)
C11B—C10B—C8	111.4 (5)	O9—C8—N4	119.78 (14)
C15B—C10B—C8	131.7 (6)	O9—C8—C10B	122.9 (6)
C10B—C11B—C12B	120.7 (7)	N4—C8—C10B	117.4 (6)
C10B—C11B—H11B	119.6	O9—C8—C10A	121.7 (4)
C12B—C11B—H11B	119.6	N4—C8—C10A	118.5 (4)
C13B—C12B—C11B	121.1 (10)	S1—C18—H18A	109.5
C13B—C12B—H12B	119.4	S1—C18—H18B	109.5
C11B—C12B—H12B	119.4	H18A—C18—H18B	109.5
C12B—C13B—C14B	120.1 (7)	S1—C18—H18C	109.5
C12B—C13B—H13B	120.0	H18A—C18—H18C	109.5
C14B—C13B—H13B	120.0	H18B—C18—H18C	109.5

C15A—C10A—C11A—C12A	1.4 (15)	N3—N4—C5—N6	−0.4 (2)
C8—C10A—C11A—C12A	−174.5 (8)	C8—N4—C5—N7	4.2 (3)
C15A—C10A—C11A—F1A	178.3 (8)	N3—N4—C5—N7	−179.8 (2)
C8—C10A—C11A—F1A	2.4 (14)	N7—C5—N6—C2	179.1 (2)
F1A—C11A—C12A—C13A	−176.6 (7)	N4—C5—N6—C2	−0.3 (2)
C10A—C11A—C12A—C13A	0.1 (14)	N4—N3—C2—N6	−1.2 (2)
C11A—C12A—C13A—C14A	0.0 (9)	N4—N3—C2—S1	177.63 (14)
C12A—C13A—C14A—C15A	−1.6 (7)	C5—N6—C2—N3	1.0 (2)

C13A—C14A—C15A—C10A	3.2 (8)	C5—N6—C2—S1	−177.93 (15)
C11A—C10A—C15A—C14A	−3.1 (12)	C18—S1—C2—N3	−1.9 (2)
C8—C10A—C15A—C14A	173.0 (6)	C18—S1—C2—N6	176.86 (17)
C15B—C10B—C11B—C12B	−8 (2)	C5—N4—C8—O9	3.3 (3)
C8—C10B—C11B—C12B	179.6 (13)	N3—N4—C8—O9	−172.11 (17)
C10B—C11B—C12B—C13B	6 (2)	C5—N4—C8—C10B	−176.2 (6)
C11B—C12B—C13B—C14B	0.0 (17)	N3—N4—C8—C10B	8.4 (6)
C12B—C13B—C14B—C15B	−3.1 (12)	C5—N4—C8—C10A	−177.5 (4)
C13B—C14B—C15B—F1B	−179.4 (8)	N3—N4—C8—C10A	7.1 (4)
C13B—C14B—C15B—C10B	0.4 (15)	C11B—C10B—C8—O9	44.0 (16)
C11B—C10B—C15B—F1B	−175.0 (13)	C15B—C10B—C8—O9	−126.6 (15)
C8—C10B—C15B—F1B	−5 (2)	C11B—C10B—C8—N4	−136.5 (11)
C11B—C10B—C15B—C14B	5 (2)	C15B—C10B—C8—N4	52.9 (19)
C8—C10B—C15B—C14B	175.4 (12)	C15A—C10A—C8—O9	−130.7 (7)
C2—N3—N4—C8	177.04 (17)	C11A—C10A—C8—O9	45.2 (11)
C2—N3—N4—C5	0.9 (2)	C15A—C10A—C8—N4	50.1 (9)
C8—N4—C5—N6	−176.37 (18)	C11A—C10A—C8—N4	−134.0 (8)

Hydrogen-bond geometry (Å, º)

D—H···*A*	*D*—H	H···*A*	*D*···*A*	*D*—H···*A*
N7—H1···O9	0.86 (1)	2.14 (2)	2.738 (2)	126 (2)
C15*A*—H15*A*···N3	0.93	2.60	2.960 (5)	104
N7—H2···N6^{i}	0.86 (2)	2.13 (2)	2.987 (3)	174 (2)
C14*A*—H14*A*···O9^{ii}	0.93	2.36	3.275 (4)	167

Symmetry codes: (i) −*x*+3, −*y*+1, −*z*+2; (ii) *x*−1, *y*, *z*.

2-Fluoro-*N*-(3-methylsulfanyl-1*H*-1,2,4-triazol-5-yl)benzamide (Compound_4)

Crystal data

$C_{10}H_9FN_4OS$
M_r = 252.27
Monoclinic, $P2_1/n$
a = 5.0509 (11) Å
b = 26.640 (5) Å
c = 8.0251 (16) Å
β = 94.12 (2)°
V = 1077.0 (4) Å^3
Z = 4
$F(000)$ = 520
D_x = 1.556 Mg m^{-3}
Mo $K\alpha$ radiation, λ = 0.71073 Å
Cell parameters from 3138 reflections
θ = 4.0–24.7°
μ = 0.30 mm^{-1}
T = 298 K
Parallelepiped, colorless
0.23 × 0.08 × 0.05 mm

Data collection

Agilent SuperNova Dual Source diffractometer with an Atlas detector
Radiation source: SuperNova (Mo) X-ray Source
Detector resolution: 5.3072 pixels mm^{-1}
ω scans
Absorption correction: multi-scan (CrysAlis PRO; Agilent, 2014)
T_{min} = 0.734, T_{max} = 1.000
5060 measured reflections
5060 independent reflections
3267 reflections with $I > 2\sigma(I)$
R_{int} = 0.080
θ_{max} = 26.8°, θ_{min} = 3.1°
h = −6→6
k = −33→33
l = −9→9

Refinement

Refinement on F^2
Least-squares matrix: full
$R[F^2 > 2\sigma(F^2)] = 0.071$
$wR(F^2) = 0.237$
$S = 1.10$
5060 reflections
165 parameters
0 restraints
Primary atom site location: iterative
Secondary atom site location: difference Fourier map
Hydrogen site location: mixed
H atoms treated by a mixture of independent and constrained refinement
$w = 1/[\sigma^2(F_o^2) + (0.1329P)^2]$
where $P = (F_o^2 + 2F_c^2)/3$
$(\Delta/\sigma)_{max} = 0.001$
$\Delta\rho_{max} = 0.29$ e Å^{-3}
$\Delta\rho_{min} = -0.37$ e Å^{-3}

Special details

Geometry. All esds (except the esd in the dihedral angle between two l.s. planes) are estimated using the full covariance matrix. The cell esds are taken into account individually in the estimation of esds in distances, angles and torsion angles; correlations between esds in cell parameters are only used when they are defined by crystal symmetry. An approximate (isotropic) treatment of cell esds is used for estimating esds involving l.s. planes.
Refinement. Refined as a 3-component twin

Fractional atomic coordinates and isotropic or equivalent isotropic displacement parameters (Å²)

	x	*y*	*z*	U_{iso}*/U_{eq}
S1	0.1477 (4)	0.27586 (4)	0.0007 (2)	0.0449 (5)
F1	0.1660 (7)	0.53895 (10)	0.1032 (4)	0.0505 (9)
H1	0.223 (15)	0.461 (2)	0.206 (8)	0.06 (2)*
O1	0.8265 (8)	0.46221 (12)	0.2805 (5)	0.0404 (10)
N1	0.5883 (9)	0.32664 (13)	0.1083 (6)	0.0357 (11)
C1	0.4195 (13)	0.23505 (19)	−0.0417 (9)	0.0544 (18)
H1A	0.351155	0.204771	−0.093496	0.082*
H1B	0.519322	0.226953	0.061054	0.082*
H1C	0.532742	0.251692	−0.115383	0.082*
C2	0.3270 (11)	0.32716 (16)	0.0838 (6)	0.0303 (11)
N2	0.6408 (10)	0.37462 (14)	0.1623 (6)	0.0344 (11)
C3	0.4156 (10)	0.40049 (16)	0.1636 (6)	0.0301 (12)
N3	0.2102 (9)	0.37196 (14)	0.1168 (6)	0.0358 (11)
C4	0.6041 (11)	0.48003 (17)	0.2559 (6)	0.0307 (12)
H4	0.81 (2)	0.386 (3)	0.187 (12)	0.11 (3)*
N4	0.3965 (9)	0.45071 (14)	0.1992 (6)	0.0342 (10)
C6	0.3445 (12)	0.56183 (17)	0.2127 (7)	0.0361 (13)
C5	0.5514 (10)	0.53388 (16)	0.2864 (6)	0.0305 (12)
C7	0.3142 (13)	0.61226 (18)	0.2366 (7)	0.0448 (15)
H7	0.173297	0.629657	0.182589	0.054*
C9	0.7035 (14)	0.60997 (19)	0.4223 (8)	0.0497 (16)
H9	0.824367	0.626244	0.496651	0.060*
C8	0.4989 (14)	0.63664 (19)	0.3431 (8)	0.0520 (17)
H8	0.484520	0.670992	0.361139	0.062*
C10	0.7318 (12)	0.55995 (18)	0.3933 (7)	0.0388 (13)
H10	0.874783	0.542851	0.446041	0.047*

Atomic displacement parameters (Å²)

	U^{11}	U^{22}	U^{33}	U^{12}	U^{13}	U^{23}
S1	0.0279 (8)	0.0374 (7)	0.0688 (11)	−0.0045 (6)	−0.0013 (7)	−0.0100 (6)
F1	0.044 (2)	0.0498 (17)	0.055 (2)	0.0030 (15)	−0.0163 (17)	0.0033 (15)
O1	0.025 (2)	0.0422 (19)	0.053 (2)	0.0033 (16)	−0.0032 (18)	−0.0046 (16)
N1	0.027 (3)	0.033 (2)	0.047 (3)	−0.0011 (18)	0.004 (2)	−0.0006 (18)
C1	0.040 (4)	0.043 (3)	0.082 (5)	0.001 (3)	0.009 (4)	−0.019 (3)
C2	0.019 (3)	0.035 (2)	0.037 (3)	0.000 (2)	0.001 (2)	0.001 (2)
N2	0.020 (3)	0.034 (2)	0.049 (3)	0.0007 (19)	0.002 (2)	−0.0024 (18)
C3	0.024 (3)	0.033 (2)	0.034 (3)	0.004 (2)	−0.001 (2)	0.000 (2)
N3	0.024 (3)	0.033 (2)	0.051 (3)	−0.0016 (18)	0.005 (2)	−0.0025 (19)
C4	0.026 (3)	0.035 (2)	0.031 (3)	−0.003 (2)	0.005 (2)	−0.002 (2)
N4	0.018 (3)	0.036 (2)	0.050 (3)	0.0030 (19)	0.005 (2)	−0.0010 (18)
C6	0.037 (4)	0.037 (3)	0.036 (3)	−0.003 (2)	0.010 (3)	0.003 (2)
C5	0.028 (3)	0.035 (2)	0.028 (3)	−0.002 (2)	0.006 (2)	0.002 (2)
C7	0.044 (4)	0.044 (3)	0.048 (4)	0.007 (3)	0.015 (3)	0.010 (2)
C9	0.056 (5)	0.045 (3)	0.049 (4)	−0.012 (3)	0.007 (3)	−0.006 (3)
C8	0.065 (5)	0.036 (3)	0.058 (4)	−0.002 (3)	0.021 (3)	−0.002 (3)
C10	0.033 (4)	0.045 (3)	0.038 (3)	−0.004 (2)	0.004 (3)	−0.007 (2)

Geometric parameters (Å, º)

S1—C2	1.746 (5)	C4—N4	1.360 (7)
S1—C1	1.803 (6)	C4—C5	1.483 (7)
F1—C6	1.357 (6)	N4—H1	0.93 (7)
O1—C4	1.222 (6)	C6—C7	1.367 (7)
N1—C2	1.320 (7)	C6—C5	1.381 (7)
N1—N2	1.370 (6)	C5—C10	1.391 (7)
C1—H1A	0.9600	C7—C8	1.381 (9)
C1—H1B	0.9600	C7—H7	0.9300
C1—H1C	0.9600	C9—C10	1.362 (7)
C2—N3	1.366 (6)	C9—C8	1.372 (9)
N2—C3	1.331 (7)	C9—H9	0.9300
N2—H4	0.90 (10)	C8—H8	0.9300
C3—N3	1.319 (7)	C10—H10	0.9300
C3—N4	1.373 (6)		
C2—S1—C1	99.4 (3)	C4—N4—C3	124.4 (5)
C2—N1—N2	101.9 (4)	C4—N4—H1	121 (4)
S1—C1—H1A	109.5	C3—N4—H1	113 (4)
S1—C1—H1B	109.5	F1—C6—C7	117.2 (5)
H1A—C1—H1B	109.5	F1—C6—C5	118.8 (4)
S1—C1—H1C	109.5	C7—C6—C5	124.0 (5)
H1A—C1—H1C	109.5	C6—C5—C10	115.9 (4)
H1B—C1—H1C	109.5	C6—C5—C4	126.2 (5)
N1—C2—N3	114.9 (4)	C10—C5—C4	117.9 (5)
N1—C2—S1	122.3 (3)	C6—C7—C8	118.1 (6)

N3—C2—S1	122.6 (4)	C6—C7—H7	120.9
C3—N2—N1	109.8 (4)	C8—C7—H7	120.9
C3—N2—H4	128 (5)	C10—C9—C8	120.8 (6)
N1—N2—H4	122 (5)	C10—C9—H9	119.6
N3—C3—N2	110.8 (4)	C8—C9—H9	119.6
N3—C3—N4	123.7 (5)	C9—C8—C7	119.7 (5)
N2—C3—N4	125.4 (5)	C9—C8—H8	120.1
C3—N3—C2	102.5 (4)	C7—C8—H8	120.1
O1—C4—N4	120.6 (4)	C9—C10—C5	121.4 (5)
O1—C4—C5	121.5 (5)	C9—C10—H10	119.3
N4—C4—C5	117.9 (5)	C5—C10—H10	119.3
N2—N1—C2—N3	0.6 (6)	F1—C6—C5—C10	178.1 (5)
N2—N1—C2—S1	176.0 (4)	C7—C6—C5—C10	1.4 (8)
C1—S1—C2—N1	−3.9 (5)	F1—C6—C5—C4	1.2 (8)
C1—S1—C2—N3	171.2 (4)	C7—C6—C5—C4	−175.5 (5)
C2—N1—N2—C3	−1.3 (5)	O1—C4—C5—C6	155.9 (5)
N1—N2—C3—N3	1.6 (6)	N4—C4—C5—C6	−24.1 (7)
N1—N2—C3—N4	−175.0 (4)	O1—C4—C5—C10	−21.0 (7)
N2—C3—N3—C2	−1.2 (5)	N4—C4—C5—C10	159.0 (5)
N4—C3—N3—C2	175.5 (5)	F1—C6—C7—C8	−177.9 (5)
N1—C2—N3—C3	0.3 (6)	C5—C6—C7—C8	−1.2 (8)
S1—C2—N3—C3	−175.0 (4)	C10—C9—C8—C7	2.0 (9)
O1—C4—N4—C3	−0.8 (8)	C6—C7—C8—C9	−0.6 (9)
C5—C4—N4—C3	179.2 (4)	C8—C9—C10—C5	−1.7 (9)
N3—C3—N4—C4	176.4 (5)	C6—C5—C10—C9	0.0 (8)
N2—C3—N4—C4	−7.4 (8)	C4—C5—C10—C9	177.2 (5)

Hydrogen-bond geometry (Å, º)

D—H···*A*	*D*—H	H···*A*	*D*···*A*	*D*—H···*A*
N4—H1···F1	0.92 (7)	2.25 (6)	2.710 (5)	111 (5)
N2—H4···O1	0.92 (10)	2.16 (8)	2.664 (5)	114 (7)
N4—H1···O1^{i}	0.92 (7)	2.13 (8)	3.013 (6)	159 (5)
N2—H4···N3^{ii}	0.92 (10)	2.17 (10)	2.926 (7)	140 (8)
C10—H10···O1^{iii}	0.93	2.58	3.367 (7)	143
C1—H1*A*···N1^{iv}	0.96	2.78	3.566 (8)	140

Symmetry codes: (i) *x*−1, *y*, *z*; (ii) *x*+1, *y*, *z*; (iii) −*x*+2, −*y*+1, −*z*+1; (iv) *x*−1/2, −*y*+1/2, *z*−1/2.